

Momentum Balance Across a Barrier Reef

D. Sous^{1,2} , G. Dodet³ , F. Bouchette^{4,5} , and M. Tissier⁶ 

Key Points:

- The first complete evaluation of momentum balance over a reef barrier from measurements and numerical modeling
- Reef hydrodynamics evolves from classical beach regime on the forereef to a friction-driven flow over the reef flat
- Wave resolving numerical simulations highlight the complexity of the vertical structure of the flow

Correspondence to:

D. Sous,
sous@univ-tln.fr

Citation:

Sous, D., Dodet, G., Bouchette, F., & Tissier, M. (2020). Momentum balance across a barrier reef. *Journal of Geophysical Research: Oceans*, 125, e2019JC015503. <https://doi.org/10.1029/2019JC015503>

Received 19 JUL 2019

Accepted 1 FEB 2020

Accepted article online 7 FEB 2020

¹Mediterranean Institute of Oceanography (MIO), Université de Toulon, Aix Marseille Université, CNRS, IRD, La Garde, France, ²Univ Pau & Pays Adour / E2S UPPA, Chaire HPC-Waves, Laboratoire des Sciences de l'Ingénieur Appliquées à la Mécanique et au Génie Electrique Fédération IPRA, ANGLET, France, ³IFREMER, Univ. Brest, CNRS, IRD, Laboratoire d'Océanographie Physique et Spatiale (LOPS), IUEM, Brest, France, ⁴Geosciences-Montpellier, Univ Montpellier, CNRS, Montpellier, France, ⁵GLADYS, Le Grau du Roi, Occitanie, France, ⁶Environmental Fluid Mechanics Section, Faculty of Civil Engineering and Geosciences, Delft University of Technology, Stevinweg 1, Delft, The Netherlands

Abstract This paper reports on a combined experimental and numerical study dedicated to barrier reefs hydrodynamics. A network of pressure sensors and velocity profilers has been deployed for more than 2 months over the Ouano reef barrier, New Caledonia. The primary aim of the study is to assess the relevance of the classical depth-averaged momentum balance in such a complex and poorly documented environment. The combined analysis of experimental and numerical measurements reveals a specific hydrodynamic behavior contrasting with sandy beaches and fringing reefs. The cross-reef current induced by wave breaking over the barrier reef plays an important role in the momentum budget, in particular through friction processes. The hydrodynamic behavior over the barrier reef is thus characterized by the progressive transition from a nearly classical beach type behavior on the forereef, where the gradient of radiation stress is balanced by a barotropic pressure gradient associated to the wave setup, to an open-channel type regime, dominated by frictional head loss. The reef top wave setup shows a clear depth dependency mainly attributed to the forereef curvature. During extreme wave events, the measurements tend to indicate a transition toward a critical hydraulic regime above the reef top. The numerical simulations, involving a non-hydrostatic wave-resolving model coupled to a $K - \epsilon$ turbulence model, highlight the vertical structure of the flow. Over the reef flat, a classical log-layer profile is observed, in agreement with measurements, while above the forereef an anticlockwise circulation develops under the breaking zone.

1. Introduction

Coral reefs are facing a global degradation caused by ocean acidification and warming associated with increasing greenhouse gas emission and water pollution due to the growing anthropic pressure. Two major consequences of reef degradation are the increase of wave-driven flooding events (Storlazzi et al., 2015) and the deterioration of reef ecosystems and biological productivity. Improving the resilience of coral reefs is of primary importance for coral reef coasts in general and more particularly for small island developing states that are vulnerable territories with often limited capacity for coastal mitigation solutions. The health of reef-lagoon ecosystems is directly dependent on the hydrodynamical functioning which controls the exchanges with the open ocean, the renewal of water masses, and the fluxes of nutrients, sediments, and contaminants.

The hydrodynamics of nearshore systems are mainly governed by the coupling between wave action, water level, circulation and bottom friction. These processes are linked to each other within coupled wave-circulation numerical models through the depth-averaged momentum balance equation (Dodet et al., 2013; Roelvink et al., 2009). In coral reef environments, waves are often a major contributor to the momentum balance, affecting water level fluctuations and overall circulation within the lagoon or at the shore (Andréfouët et al., 2001; Angwenyi & Rydberg, 2005; Chevalier et al., 2014, 2015; Hench et al., 2008; Hoeke et al., 2013; Kench & McLean, 2004; Kraines et al., 1998, 1999; Lowe et al., 2009; Pomeroy et al., 2017; Sous et al., 2017; Taebi et al., 2011; Tartinville & Rancher, 2000; Wolanski et al., 1993). Recently, a diligent research effort has therefore been engaged to better understand wave transformation over coral reefs, in particular for fringing reefs (Gawehn et al., 2016; Monismith et al., 2013; Péquignet et al., 2011; Roeber & Cheung, 2012; Van Dongeren et al., 2013; Vetter et al., 2010).

The present study aims to assess the depth-averaged momentum balance across barrier reefs. To better discriminate each of the processes involved, the simplest case of a purely cross-shore system under stationary wave forcing is discussed below. Under the assumption of steady flow and normally incident wave forcing averaged over many wave cycles, the depth-averaged alongshore uniform cross-shore momentum equation can be written as (Buckley et al., 2015; Gourlay & Colleter, 2005)

$$\frac{\partial}{\partial x}(\rho U^2) = -g\rho \frac{\partial \bar{\eta}}{\partial x} - \frac{1}{(\bar{\eta} + h)} \frac{\partial S_{xx}}{\partial x} - \frac{1}{(\bar{\eta} + h)} \bar{\tau}_b, \quad [Pa.m^{-1}], \quad (1)$$

where U is the depth-averaged velocity, g the gravitational acceleration, ρ the water density, $\bar{\eta}$ the wave setup, h the still water depth, S_{xx} the radiation stress, and τ_b the bed shear stress. In the following, these four terms will be referred to as, from the left to the right in equation (1), the advection, slope, radiation, and friction terms. In fringing reef systems, the shore imposes theoretically a zero net depth-averaged transport across the reef. The depth-averaged momentum balance therefore reduces to the classical sandy beach form, although the friction term, due to waves and possibly to the offshore-directed near-bed mean velocity (Buckley et al., 2016), plays a more prevailing role because of the generally high reef roughness. In their analysis of multiple fringing reefs, Vetter et al. (2010) and Becker et al. (2014) observed that the setup displays a nearly linear dependency on incoming wave height with a maximal magnitude similar to the range observed on sandy beaches, that is, 15 – 20 % of the offshore wave height (Guza & Thornton, 1981).

A number of analytical models derived from equation (1) with various degrees of simplification have been proposed and tested against field and laboratory data in reef contexts (Becker et al., 2014; Bonneton et al., 2007; Buckley et al., 2015, 2016; Gourlay & Colleter, 2005; Hearn, 1999; Massel & Gourlay, 2000; Monismith et al., 2013; Symonds et al., 1995; Vetter et al., 2010). A key characteristic of barrier reefs hydrodynamics, which are much less documented than fringing reef hydrodynamics, is that the gradient of radiation stress due to wave breaking induces a barotropic pressure gradient driving a net cross-shore current U across the barrier (Bonneton et al., 2007; Gourlay & Colleter, 2005; Hearn, 1999; Lowe et al., 2005; Lugo-Fernández et al., 1998; Monismith, 2007). This flow is expected to strongly affect the momentum balance by enhancing the friction term and, in the presence of strong bathymetric variations, the advection term.

Extending the analysis on wave transformation over barrier reef carried out by Sous et al. (2019), the present study uses dedicated field measurements in order to investigate the depth-averaged momentum balance across barrier reefs. The approach builds on the observations of momentum dynamics carried out on coral reef systems (Hench et al., 2008; Lentz et al., 2016, 2017; Lowe et al., 2009; Monismith et al., 2013). The specific focus is here to quantify the spatial variations of each momentum flux term in equation (1) across a well-defined barrier reef and to examine the dependency of these terms on water level and wave forcing. In order to complete and extend the studied area, a series of numerical simulations is performed using a multilayer wave-resolving model. These numerical simulations are also used to characterize the vertical structure of the flow and as such assess the limitations of the depth-averaged approach.

The Ouano barrier reef, New Caledonia, has been selected as study site because it is one of the most archetypal reef barrier system of the South Pacific coasts, with a wide, regular and rectilinear reef barrier separated from the land by a well-developed lagoon (Sous et al., 2017). Furthermore, it is exposed to consistent long swell forcing with a nearly reef normal incidence generating cross-reef wave-induced transport over the barrier. The Ouano site provides thus a generic framework to study barrier reef hydrodynamics. The first part of the manuscript is dedicated to a short presentation of the experiments and methods which are described in more details in Sous et al. (2019). The second part describes the field results while additional insight on the studied processes is provided by numerical modeling in the discussion section. The last section is dedicated to conclusions and prospects.

2. Experiments

2.1. Field Survey

This work uses a data set part of a large hydro-biogeochemical field campaign (OLZO and CROSS-REEF projects) conducted from mid-April to July, 2016. The studied site is the Ouano reef-lagoon system, South-West New Caledonia. It is a coastal weakly anthropized lagoon, nearly 30 km long, 10 km wide, and 10 m deep, exposed to micro tides (tidal range 1.7 m) and south Pacific swells, which can be classified

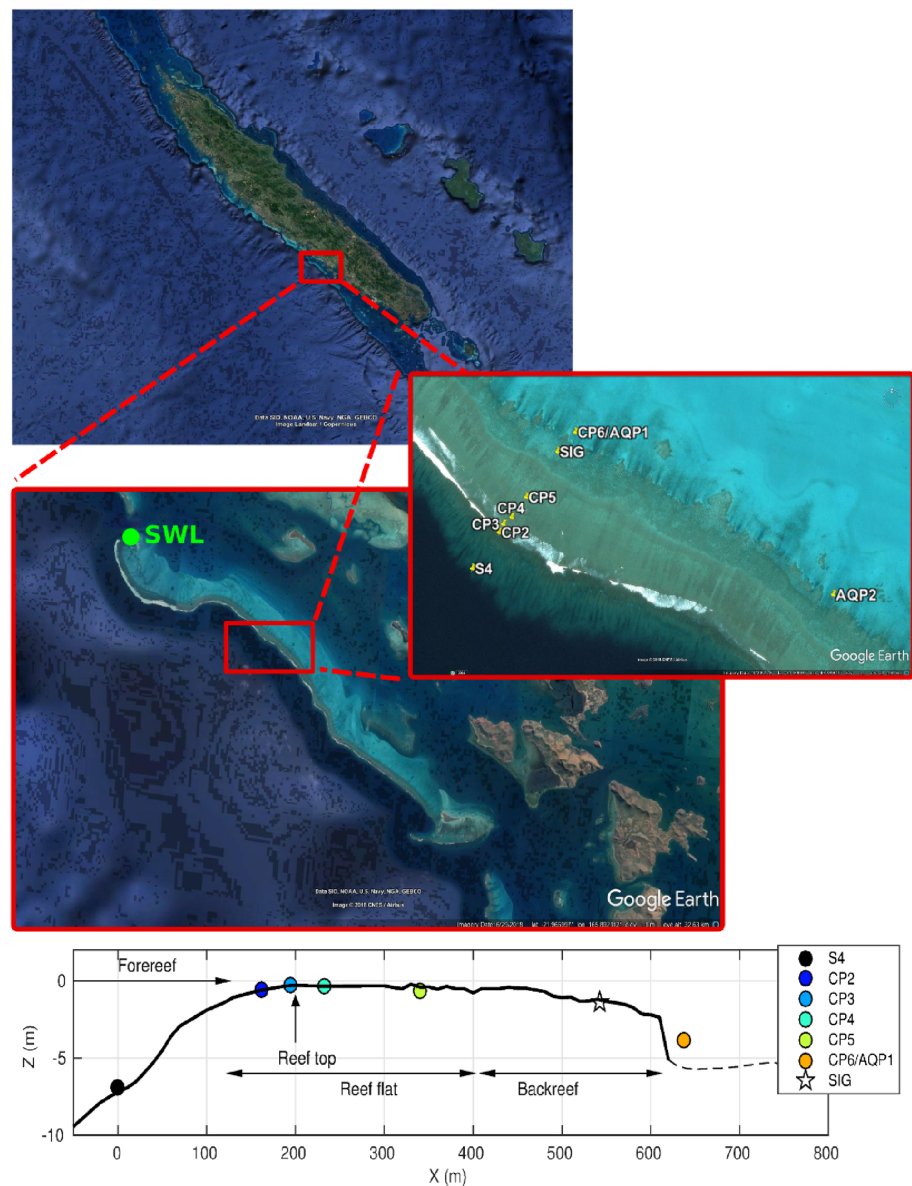


Figure 1. Bathymetric profile and instrumentation across the studied transect. Reef and sand bottom are shown in solid and dashed line. The still water level (SWL) is measured in the Isié passage, in 19-m depth, about 9 km away from the studied transect.

as a channel lagoon (Sous et al., 2017). Further details on the lagoon functioning are reported elsewhere (Chevalier et al., 2015; Locatelli et al., 2017; Sous et al., 2017, 2019).

Most of the instrumentation considered here was deployed on a single cross-reef transect (Figure 1). Incoming wave conditions are provided by an S4 electro-current meter deployed on the reef foreshore, in 7.3-m depth, recording 20-min bursts of data every 3 hr. Five pressure sensors were bottom-mounted across the reef barrier to monitor wave and mean water levels. CP2 to CP5 are OSS1-010-003[®] wave gauges and CP6 is an RBR Duo[®] recording continuously at 5 and 2 Hz, respectively. The effect of dynamic pressure, in particular related to the flow blockage by the sensor (Bernoulli effect), has been minimized by avoiding the direct exposure of the sensor membrane to the main current and wave orbital velocities. The pressure sensors were therefore, (i) oriented as far as possible in alongshore direction, (ii) placed in reef grooves, and (iii) protected by a stainless grid (1-mm mesh). The remaining influence of dynamical pressure on the MWL calculation, that is, after 40-min time averaging, is therefore expected to be negligible except maybe for the shallower water depths. The still water level (SWL), defined in the local hydrographic datum (EPSG:5151),

was obtained by a bottom moored pressure measurement (RBR Duo[®] sampling at 2 Hz) in the Isié passage located about 9 km from the studied transect (see Figure 1). This measurement point was sheltered from wave action, in 19-m depth.

For each sensor, the mean water levels were computed from the continuous records subdivided in 40-min bursts. In order to correct for the long-term drifting error of the sensor during the survey period, we used the residuals between the atmospheric pressure measured at Tontouta airport and the measured pressure just before and after immersion. For each of the sensors, it remained smaller than 2 cm. Linear corrections were then applied to remove the long-term drift for each sensor.

When possible, instruments were positioned by DGPS (Differential Global Positioning System). Sensors CP4 and CP5, which were the most accessible ones, have been repeatedly positioned at low tide during the calmest conditions encountered in the April-July period. They are used as reference for vertical positioning of the other instruments. It is here assumed that in the absence of waves and currents, the mean water level should be the same at each sensor. The difference between mean water levels at the selected and the reference sensors has been plotted (not shown here) against the incoming wave height for the entire campaign. The vertical position of the selected sensor was then adjusted to ensure that this difference tends to zero for zero incoming wave height. This procedure was first applied to the Isié sensor to obtain its vertical position and therefore determine the SWL. The vertical position of sensors CP2, CP3 and CP6 was then adjusted with respect to the SWL using the same procedure. The overall uncertainty on the free surface elevation (2.5 cm) is estimated as the standard deviation of the difference between mean water level for a given sensor and SWL in non-breaking conditions ($H_s < 0.8$ m). Note that a small tidal shift is present between the SWL measurement point and the instrumented transect. Numerical tests, based on the ROMS/CROCO regional model configuration used by Chevalier et al. (2015), showed that the difference between mean water levels measured at the Isié point used here and at an off-reef point aligned with the instrumented transect roughly ranges between 0.5 and 1.5 cm, which remains in the overall uncertainty of free surface level measurements. The still water depth over the reef top SWL_r is finally obtained by subtracting the reef top elevation from the SWL.

Velocity profiles were measured by acoustic Doppler current profilers at three locations of the reef: AQP1, AQP2, and SIG. AQP1 and the five pressure sensors were measuring during the whole campaign from 11 April to 30 June while S4 wave measurements started 2 weeks later on 25 April. AQP2 and SIG have been deployed for shorter periods, about 2 weeks each. AQP1 and AQP2 profilers are Nortek Aquadopp deployed at the toe of the morphologic step, which marks the end of the barrier around $X = 610$ m (Figure 1). This ensures that the cross-reef current was measured for the whole tidal cycle, that is, even for the very shallow water depth observed on the reef top at low tide which are unreachable by current meters deployed at or near the reef top. AQP1 is nearly aligned with the network of pressure sensors while AQP2 is deployed at the same cross-shore position but shifted 1.1 km south-eastward to characterize the along-reef variability. Both profilers recorded 60 s time-averaged velocity profiles with 20 cm cells each 1, 200 s. Due to the instrument length and top-looking orientation, the lowest measurement cell for AQP1 and AQP2 is about 1.15 m above the bottom. A third high-resolution Nortek Signature 1000 profiler (SIG) has been deployed above the back-reef to study the vertical structure of velocity during 20-min bursts in 3-cm cells at 4 Hz. The SIG profiler has been positioned in a small depression of the reef colony so that the first measurement cell is nearly 31 cm above the surrounding canopy. In addition to the velocity profile, the SIG profiler gives access to the local pressure and a direct acoustic measurement of the free surface. For each profiler, the measured velocities are projected into the reef main axis to obtain the cross and along-reef components. Positive values of cross-reef and along-reef components correspond to northward (water entering the lagoon) and westward currents, respectively. The calculation of depth-averaged currents and transports is performed after extending the velocity profile over the entire water column. The upper acoustic Doppler current profilers cell affected by side-lobe reflection is removed and replaced by the values obtained from linear extrapolation of the underlying 0.5-m layer. The velocity profile is then extended to a zero bottom velocity (no-slip condition) using second-order polynomial extrapolation. The reader is referred to Sous et al. (2019) for further details on the experiments.

2.2. Evaluation of Momentum Fluxes

Each term of the momentum balance (equation 1) is estimated from the field data at three positions between the consecutive pressure sensors CP2-CP3, CP3-CP4, and CP4-CP5. The analysis is performed over continuous records subdivided in 40-min bursts. Only bursts with a minimal reef top depth of 0.15 m are considered in the analysis.

2.2.1. Slope Term

The slope term $-g\rho\frac{\partial\bar{\eta}}{\partial x}$ is computed from the mean water level measured at each sensor. A negative slope term at a given location corresponds to a local positive mean surface slope along a landward oriented frame. Uncertainties in the slope term computation are mostly related to the accuracy of the vertical positioning of the instruments and the distance between the sensors used for the gradient calculation. Considering typical ranges of setup and horizontal distance of 0.2 ± 0.025 m and 50 ± 0.05 m, uncertainty on the slope term is estimated around $6 \text{ N}\cdot\text{m}^{-3}$. In addition, the measurements may also be affected by the presence of very low frequency motions across the reef barrier (Sous et al., 2019) that may add fluctuations in the estimation of free surface gradients and dynamic pressure effects, in particular for the most exposed sensor (CP2).

2.2.2. Advection Term

The advection term $\frac{\partial}{\partial x}(\rho U^2)$ is computed across the profile from the time-averaged depth-averaged transport (hereafter referred to as transport) measured at AQP1. The assumption is made that the cross-shore transport is conserved across the reef barrier (see details in section 3.1). The depth-averaged current U at each selected point is computed by dividing the transport by the local water depth, taken as the difference between mean water level and bed elevation. Considering typical ranges of transport, water depth and horizontal distances of $0.5 \pm 0.05 \text{ m}^2/\text{s}$, 1 ± 0.1 m, and 50 ± 0.05 m, uncertainty on the advection term is estimated around $1 \text{ N}\cdot\text{m}^{-3}$.

2.2.3. Radiation Stress Term

The radiation stress term $-\frac{1}{(\bar{\eta}+h)}\frac{\partial S_{xx}}{\partial x}$ is estimated from bottom pressure wave height measurements using linear theory (Longuet-Higgins & Stewart, 1962). The calculation of radiation stresses performed here ignores the wave-roller effect which can affect stresses in the surf zone as shown by Buckley et al. (2015). The total water depth $(\bar{\eta} + h)$ used here and in the friction term is taken as the mean water depth between two adjacent sensors. Considering typical ranges of water depth, wave height and horizontal distances of 1 ± 0.025 m, 1 ± 0.05 m, and 50 ± 0.05 m, uncertainty on the radiation stress term is estimated around $4 \text{ N}\cdot\text{m}^{-3}$.

2.2.4. Friction Term

The friction term combines the effects of both the mean currents and the wave-induced bottom orbital velocities. A quadratic law is used to compute the total bed shear stress (Buckley et al., 2016) combining the contributions of the depth-averaged current U and the wave bottom orbital velocity u_b :

$$\tau_b = \rho C_d \overline{|U + u_b| (U + u_b)}, \quad (2)$$

where C_d is the bottom drag coefficient. This formulation is relevant in coral reef context (Lentz et al., 2018), where wave boundary layer covers a significant part of the water column (Pomeroy et al., 2017). The depth-averaged current U is estimated from the time-averaged transport at AQP1 and the local water depth as described in section 2.2.3. The horizontal component of the orbital velocity at the bottom, u_b , is estimated from the time series of instantaneous bottom pressure and therefore includes all wave components, that is, both short and infragravity waves. Assuming linear waves in shallow water, the instantaneous horizontal velocity u_b is computed from the bottom pressure P_b as

$$u_b = \frac{CP_b}{\rho g(\bar{\eta} + h)}, \quad (3)$$

where $C = (g(\bar{\eta} + h))^{1/2}$ is the wave celerity.

The bottom drag coefficient C_d is expected to depend on the water depth (Lentz et al., 2017; McDonald et al., 2006; Pomeroy et al., 2012), which varies in time and space. C_d also changes in space because of the variations of the local biotic structure of the reef colony. In the present analysis of field data, a depth-dependent but spatially uniform friction coefficient will be used (see equation 5 and section 3.2). The well-known log profile method is used to estimate the bottom drag coefficient from the SIG measurements. The log profile method has been shown to provide a good characterization of friction over coral reefs (Pomeroy et al., 2012, 2017; Reidenbach et al., 2006) assuming that local depth remains large compared to the height of the reef colony

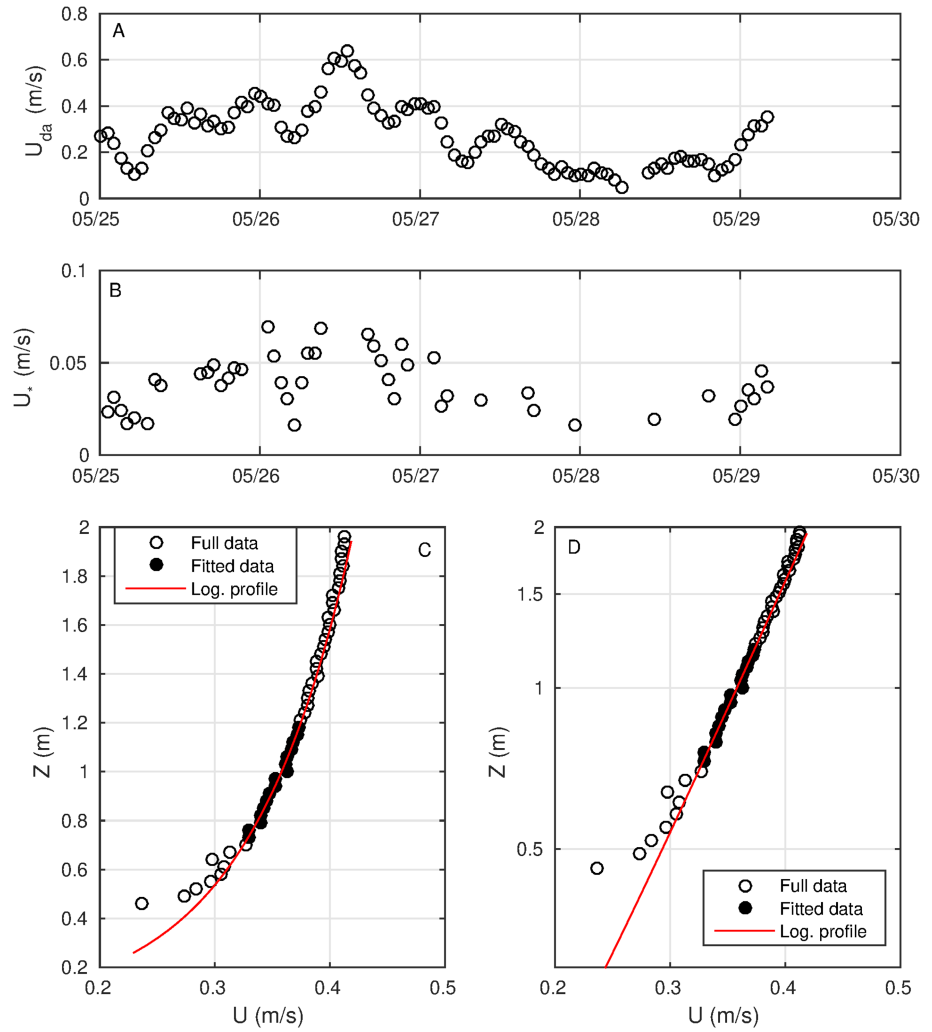


Figure 2. Log fit method to estimate the friction coefficient. Time series of depth-averaged U and friction U_* velocities are shown in panels (a) and (b), respectively. Examples of time-averaged velocity profile are given in plots (c) and (d), in linear and log scales. The complete measured profile $u(z)$ is represented by the black circles, the data used for the fit are represented by the black dots, and the resulting log fit is shown in red.

(Rosman & Hench, 2011). The SIG is located at the lower backreef (see Figure 1), quite far from the end of the surf zone, where the time-averaged velocity profile is not affected by waves.

The log profile method assumes that the vertical profile follows the canonical law of the wall:

$$u(z) = \frac{U_*}{\kappa} \ln \left(\frac{z-d}{z_0} \right), \quad (4)$$

where $u(z)$ is the time-averaged velocity profile at the elevation z above the bed, U_* is the friction velocity and $\kappa = 0.41$ is the Karman constant, and z_0 and d are the roughness and displacement heights, respectively. z_0 , d , and U_* are determined from the measured velocity profile using a least square best fit of equation (4). The fit here is applied to the lower part of the water column $0.7 < z < 1.2$ m (over 17 cells depicted with black dots in Figure 2) where the measured profiles are well described by the law of the wall. Only fits with determination coefficients above 0.9 are retained for the calculation of friction velocity. The bottom drag coefficient is then inferred from the usual quadratic law $U_*^2 = C_d U^2$. This method provides in-situ estimated values of C_d at SIG where the local depth ranges from 1.5 to 2.5 m. To extend these estimates over a larger range of depth, an analytical expression can be found for the drag coefficient by integrating the law of the

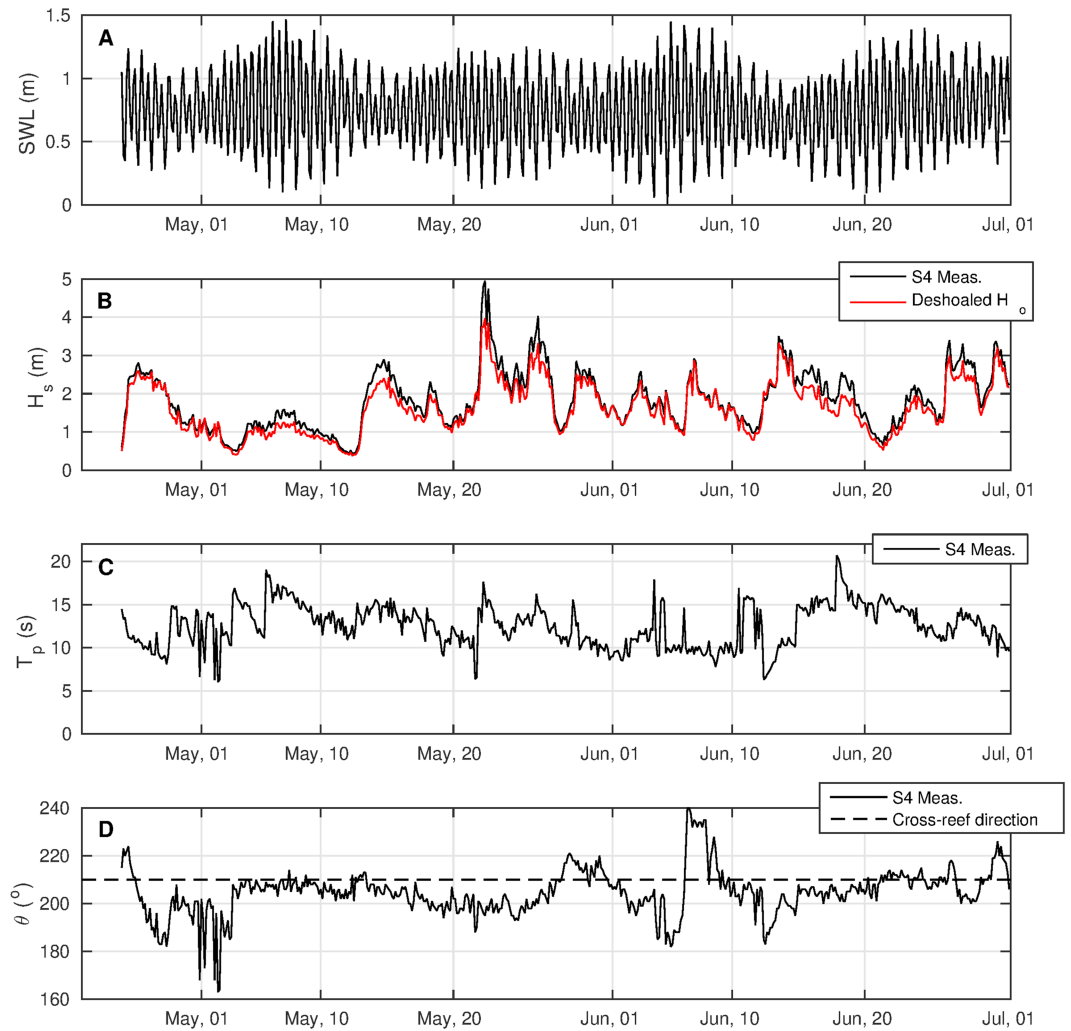


Figure 3. Hydrodynamic conditions at the S4 forereef station. (a) Still water level. (b) Significant wave heights. (c) Peak periods. (d) Wave directions in oceanographic convention with reef-normal direction in dashed line.

wall (equation 4) over the water column (Pomeroy et al., 2012):

$$C_d = \left[\frac{\kappa}{\left(\ln \left(\frac{h+\bar{\eta}-d}{z_0} \right) - 1 \right)} \right]^2. \quad (5)$$

Equation (5) will be used later on to provide an estimation of the depth dependency of C_d for each studied point across the barrier. The selected values of z_0 and d are the averaged values obtained over the whole set of log-fitted profiles. Considering typical ranges of transport, water depth, and drag coefficient of $0.5 \pm 0.05 \text{ m}^2/\text{s}$, $1 \pm 0.1 \text{ m}$, and $0.02 \pm 0.005 \text{ m}$, uncertainty on the friction term is estimated around $3.5 \text{ N}\cdot\text{m}^{-3}$.

2.3. Field Conditions

Figure 3 shows the wave climate during the experiments measured at the S4 forereef station. The overall climate is typical of the south-west coast of New Caledonia, as observed during previous experiments (Sous et al., 2017). The Ouano reef is mainly exposed to long South Pacific swell waves, with mean significant wave height of 1.8 m and mean peak period about 12.5 s, hitting the coast with a nearly reef-normal incidence. Local winds are predominantly trade winds modulated by thermal breeze and nearly aligned with the lagoon longitudinal axis, with typical peak magnitude around $5 \text{ m}\cdot\text{s}^{-1}$ reached in the afternoon. Refraction is responsible for the shore normal wave direction over the forereef (Sous et al., 2019). The SWL time series

(Figure 3a) shows the typical mesotidal regime of New Caledonia coasts, with prevalence of semidiurnal and diurnal tides M2, S2, and K1.

3. Field Results

The main aim of the field data processing is to evaluate each term of the momentum balance (equation 1). The first step of the analysis is to quantify the variability of the depth-averaged currents above the barrier, which affects both advection and friction terms. The second step is to characterize, from in situ measurements, the bottom drag coefficient involved in the friction term. Then, the spatial variations of the momentum fluxes across the barrier are explored together with their dependencies to tide and wave forcing. Last, a particular focus is put on the wave setup at the reef top, taken here as a global measurement of the difference between reef top and offshore mean water levels.

3.1. Transports and Currents

The field data set analysis is first devoted to transport and depth-averaged currents above the reef barrier, where most of the water mass input from the open ocean to the lagoon occurs (Sous et al., 2017). Transport is here defined as the integral of the velocity over the water column. Water density being constant, this quantity is conservative and is a direct measure of the mass flux over the barrier. Part of the present instrumentation has been designed to measure the spatial variability of transports above the reef barrier, both cross-shore between AQP1 and SIG, and alongshore between AQP1 and AQP2. Figures 4a and 4f show an overview of the cross- and along-reef transports calculated from the three current profilers. The cross-shore component is very well correlated for the three sensors as shown by the zoomed views in Figures 4b and 4c and the regressions depicted in Figures 4d and 4e. The regression slopes are 1.05 and 1.01 between AQP1 and AQP2, and AQP1 and SIG, respectively, with linear determination coefficients of 0.93 and 0.95, respectively. This supports the use of the AQP1 profiler to estimate cross-reef currents, which was the current profiler with the longest continuous recording time span and was able to capture the current across the studied transect even for the lowest water surface elevations. Mean values of depth-averaged current and corresponding transports were 0.29 and $0.53 \text{ m}^2\text{-s}^{-1}$. The maximum value of transport, which is clearly out of the typical range, was measured on 22 May. It corresponds to both high tide and very strong current conditions, about $2 \text{ m}\cdot\text{s}^{-1}$, during the strongest measured wave event ($H_o = 4 \text{ m}$).

Cross-reef transports are mainly controlled by wave forcing and tidal elevation. The relation with the incoming wave energy is qualitatively rather simple, that is, the larger the wave, the stronger the current. The role of tide is twofold. On one hand, the tidal oscillation controls the water depth above the reef and thus wave transformation and wave-induced currents. This produces the so-called tidally modulated wave-induced component of the current. On the other hand, the tide propagation within the reef-lagoon system generates pressure gradients across the barrier, which are responsible for the “true” tidal component of the current. In most of the cases, incoming waves on the Ouano reef barrier are sufficiently high to break over the reef top all along the tidal cycle. The net transport across the barrier thus results from the combination of the wave-induced and the true tidal components of the current, the former playing a more important part while incoming wave energy increases. Rare events of cross-shore transport reversal are observed when AQP1 and AQP2 record negative cross-shore transport values. For instance, such an event is observed in Figure 4a on 3 May. They occur generally under small wave conditions following a high tide, at periods for which non-breaking or partially breaking conditions are expected. The tidal component is then able to dominate the cross-reef flow and induces the observed reversal at early ebb, with a weak offshore current above the reef barrier.

Along-reef components of transports are depicted in Figures 4f to 4j. Figure 4i shows a moderate agreement for the transports measured with AQP1 and AQP2 profilers at the toe of the reef step, with a regression slope of 0.95 and a determination coefficient of 0.59. Both stations are rather well connected in terms of current magnitude and direction. In general, the measurements performed at the toe of the reef step (AQP1 and AQP2) show stronger along-reef currents than the ones performed above the reef (SIG) (Figures 4f, 4h, and 4j). This indicates that they are rather forced by larger circulation patterns within the lagoon (Sous et al., 2017) than directly connected to the hydrodynamics above the reef barrier. This is demonstrated by the much weaker agreement found with backreef measurements (regression slope and determination coefficient of 0.25 and 0.29 between AQP1 and SIG, respectively). Above the reef, the alongshore currents are rather small ($<0.1 \text{ m}\cdot\text{s}^{-1}$) and depend on tidal elevation, with an increasing current for higher water depth, and wave

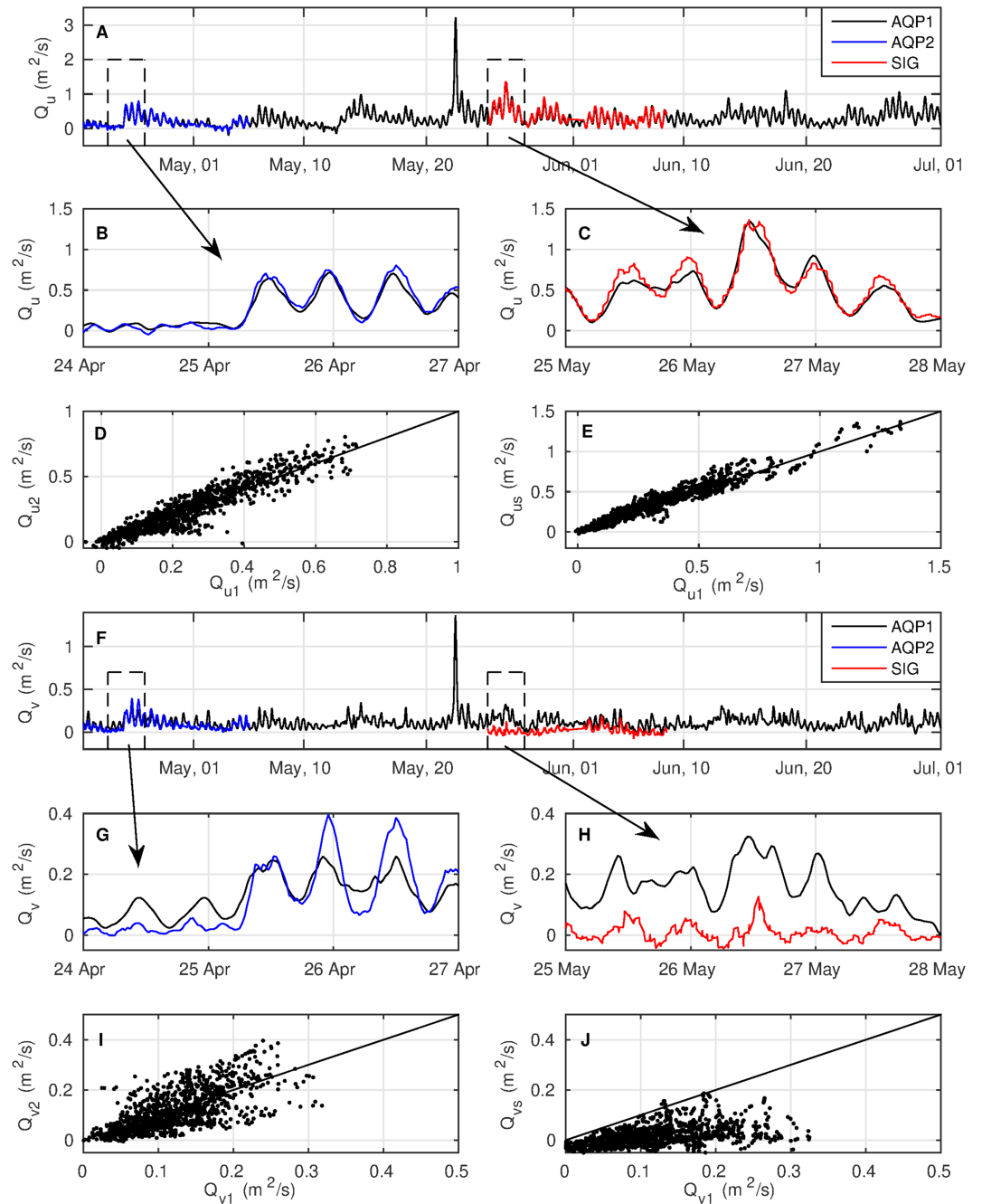


Figure 4. Measured transports for the AQP1 (black), AQP2 (blue), and SIG (red) facilities. (a,f) Full time series for cross-reef and along-reef components, respectively. (b,c,g,h) Zoomed views on selected periods for cross-reef and along-reef components, respectively. (d,e) Comparisons between cross-shore transports at AQP1 (Q_{u1}) and AQP2 (Q_{u2}), and AQP1 and SIG (Q_{us}), respectively. (i,j) Comparisons between alongshore transports at AQP1 (Q_{v1}) and AQP2 (Q_{v2}), and AQP1 and SIG (Q_{vs}), respectively.

direction, with western swells producing reef normal current while eastern swells produce stronger westward currents. A striking feature is the peak of alongshore current observed at AQP1 during the strong swell event of 22 May in Figure 4. During this event, the wave forcing is strong and oriented $\approx 200^\circ$, which generates a peculiar circulation pattern with a north-west along-reef current inside the lagoon. It has been described in more details as the Tenia reversal pattern by Sous et al. (2017). However, for the present case, the wave forcing is so strong that it drives an exceptionally intense Tenia reversal pattern event, with cross-

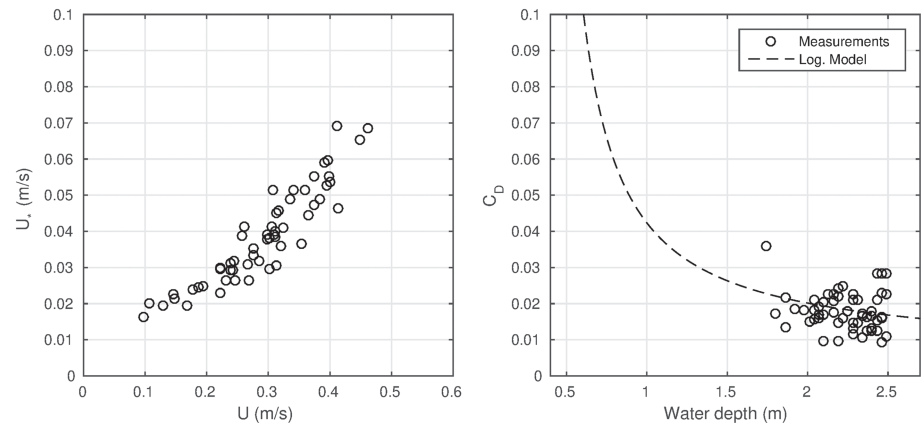


Figure 5. Comparison between field measurements of friction parameters at SIG site and comparison with theoretical prediction. Left: friction versus depth-averaged velocity. Right: comparison of the C_d depth dependency predicted by the data-fitted log model of equation (5).

and along-reef currents nearly one order of magnitude higher than the typical conditions observed during the 6 months experiment of Sous et al. (2017).

3.2. Quantification of the Bottom Friction

The bottom drag coefficient is first inferred from in situ measured velocity profiles over the backreef, see Figure 5, black circles. The mean value of C_d is 18.10^{-3} with standard deviations of 7.10^{-3} . This is in line with existing field (Pomeroy et al., 2012; Rosman & Hench, 2011) and laboratory measurements (McDonald et al., 2006). No clear depth dependency has been observed due to the rather small depth range covered by the field conditions at SIG. The mean values of z_0 and d for the duration of the experiment were 3.4 and 19.2 cm, with standard deviations of 0.75 and 1.46 cm indicating rather well-defined values. Such z_0 values are well in line with values measured in the field (Reidenbach et al., 2006; Rosman & Hench, 2011) or used in numerical models (Lowe et al., 2009; Tartinville et al., 1997).

The analytical friction model from equation (5) is then used to describe the depth dependency of the bottom drag coefficient over the complete range of depth, see Figure 5, black dashed line. The adjusted parameters z_0 and d are therefore assumed to be constant across the barrier, that is, we neglect the spatial variation of reef roughness in the estimation of momentum fluxes (Figure 6). This issue is further discussed in section 4.3.

3.3. Dynamics of the Momentum Balance

Figure 6 compares the four terms of the momentum balance (equation 1) computed from the sensors pairs CP2-CP3, CP3-CP4, and CP4-CP5 located on the reef flat, for the month of May. The curvature effects are small on the present site, such as finite differences can be used to study momentum balance across the barrier instead of complete integration of equation (1) (Lentz et al., 2016). Note that the CP5-CP6 pair is not considered here due to the steep bathymetric step at the inner barrier boundary. The advection, slope, radiation, and friction terms are plotted against the offshore wave height. The color level of each data point refers to the still water depth above the reef top (SWL_r). Despite the limitations exposed in section 2.2, comparing the evolution of the sign and of the order of magnitude of the four terms provides an interesting overview of the momentum balance across the reef barrier

First of all, it can be seen that the residual, that is, the sum of the momentum terms, is of the order of the mean measurement uncertainty (section 2.2). This means that (i) depth-averaged momentum fluxes are captured correctly and (ii) the independent contributions to the momentum flux balance considered in this paper account for most of the observed physics.

Before the reef top (CP2-CP3, left column in Figure 6), the advection term (Figure 6a), which is often assumed to be negligible in fringing reefs (Buckley et al., 2015; Gourlay, 1996; Hearn, 1999; Symonds et al., 1995), can contribute to the momentum balance up to about 15%. As expected, its contribution increases for large waves. Yet, the overall momentum balance is mainly determined by the competition between slope, radiation, and friction terms. The estimated slope term (Figure 6d) displays a significant scatter but is clearly

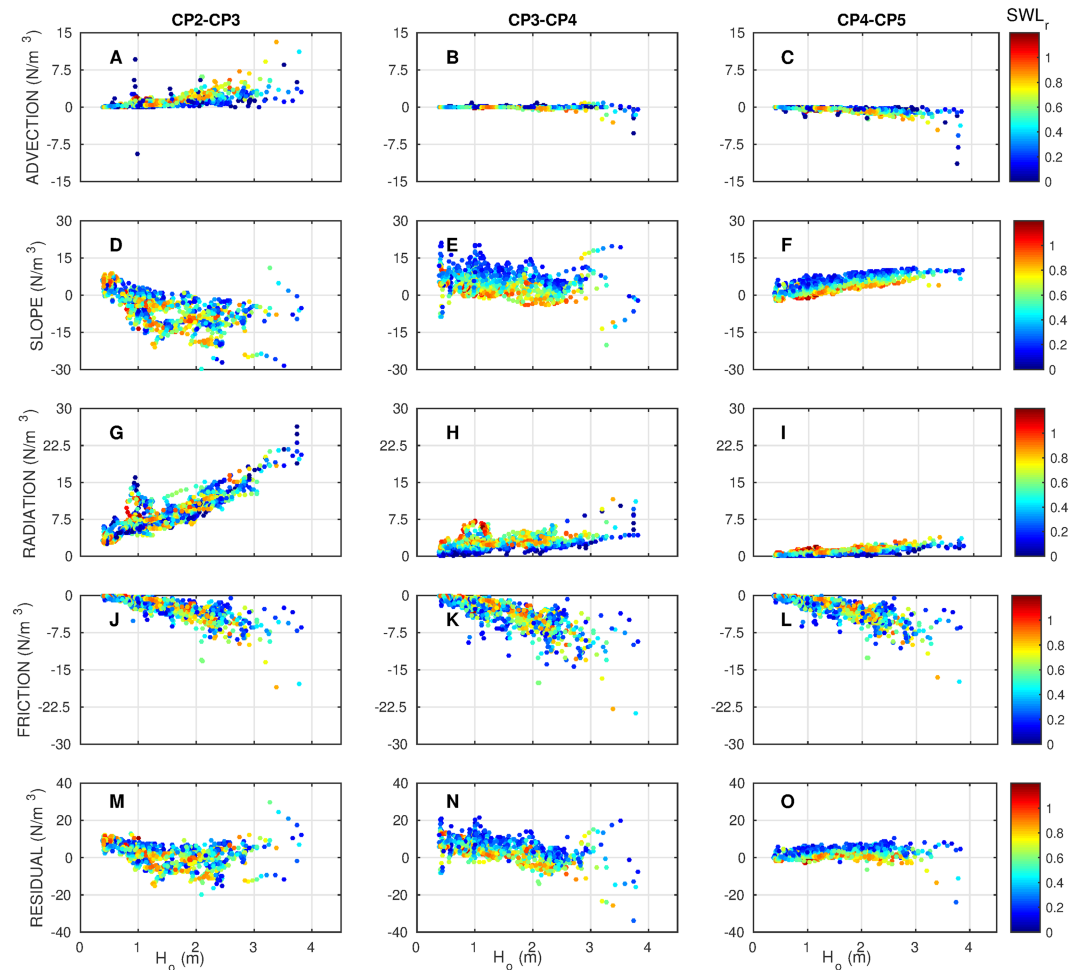


Figure 6. (a-o) Evaluation of the momentum fluxes from equation (1). Results are depicted for the three sensor pairs CP2-CP3 (left column), CP3-CP4 (middle column), and CP4-CP5 (bottom column). The four columns represent the advection, slope, radiation, and friction terms. The color levels correspond to the still water depth above the reef top.

negative, which indicates an upward tilting of the free surface in landward direction. The radiation stress term (Figure 6g) is positive as a result of the decrease in wave height, while the friction term is negative due to the onshore-directed current. The friction is here observed to play a non-negligible role on the momentum balance even within the surf zone (Figure 6j), with an order of magnitude similar to the advection term (i.e., about 10% to 15%).

At the reef top (CP3-CP4), one notes a clear change of the slope term (Figure 6e) which shows a general increase and becomes positive, that is, related to a setdown, at low tide. This trend is associated to a clear decrease of the radiation stress term (Figure 6h) and a (negative) increase of the friction term (Figure 6k). This highlights the spatial evolution of the momentum balance with a progressive shifting from wave breaking and wave setup dominated regime to a regime dominated by current-induced frictional head loss. The gradient of radiation stresses related to wave breaking from the forereef decreases across the surf zone while the friction associated to net cross-reef current progressively increases to become a dominant driver of the reef flat hydrodynamics. Such evolution highlights the specificity of barrier reefs compared to their fringing counterparts. This feature is more pronounced at low tide, when most of the short wave energy has been dissipated (and transferred to lower frequencies, Sous et al., 2019) before the reef top. At high tide, the surf zone extends beyond the reef top, and the contribution of the gradient of radiation stress remains significant in the momentum balance. Note that in our approach, the turbulence (Reynolds) stress terms (including wave-induced bottom turbulence stress, e.g., Longuet-Higgins, 2005) are not explicitly taken into account. This may explain the local imbalance between the terms of equation (1).

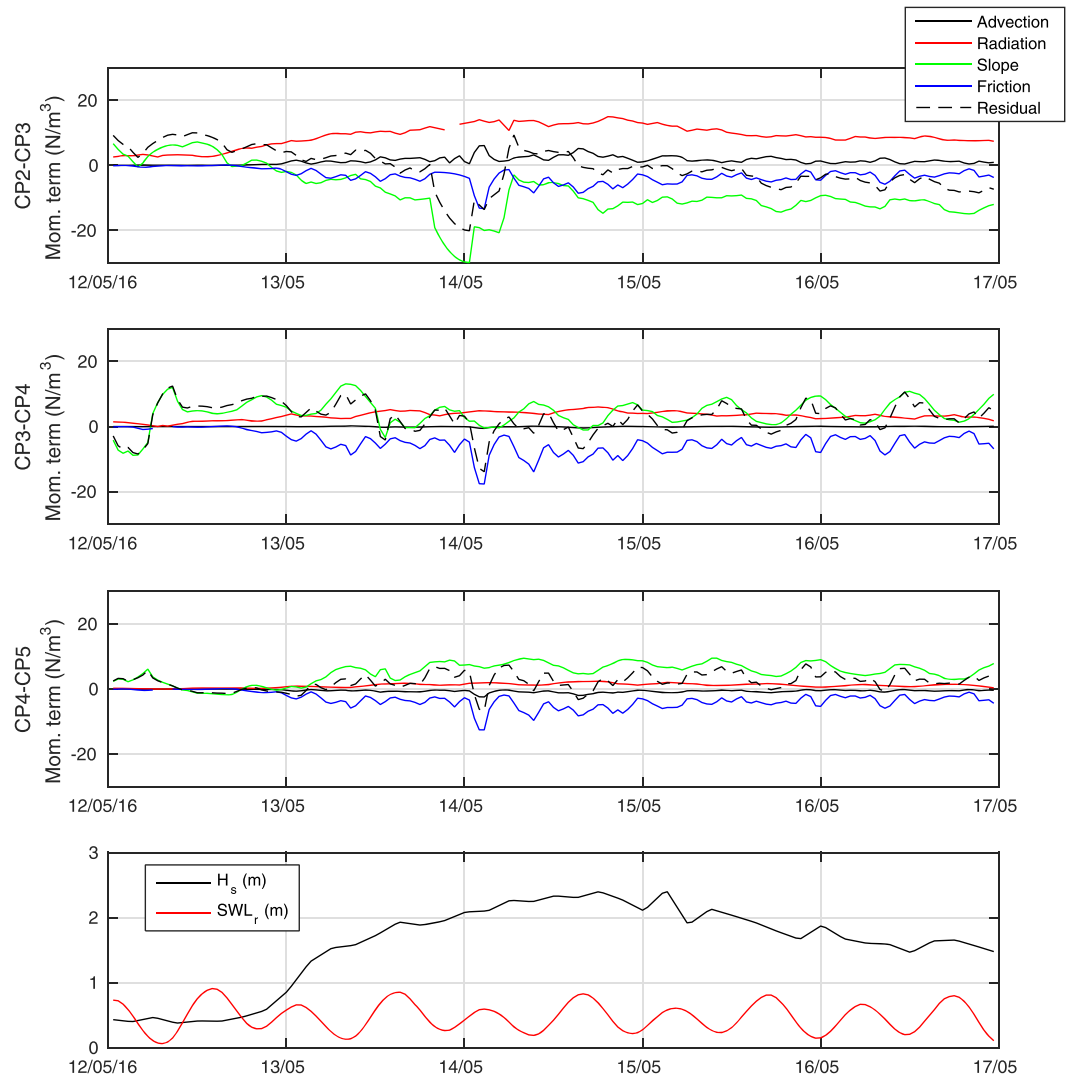


Figure 7. Time series of momentum fluxes ($\text{N}\cdot\text{m}^{-3}$) from equation (1) during a 5-day selected event. Results are depicted for the three sensor pairs CP2-CP3, CP3-CP4, and CP4-CP5. Incoming wave height and still water level above the reef top are shown in bottom plot.

Further on the backreef (CP4-CP5), the overall trend is similar. The radiation stress term (Figure 6i) is about one half the friction term (Figure 6l) while the advection term is still negligible (Figure 6c). This reveals a friction-dominated dynamics, with typical head loss of free surface flows. The slope and friction terms highlight the depth dependency of friction processes: the lower the water level, the higher the friction as predicted by equation (5).

Figure 6 presents the relationship and spread of each term of the momentum balance equation with respect to H_o and SWL. Further insight is provided in Figure 7 that compares the time series of the various terms and the residual for a selected time period (see e.g., Feddersen et al., 1998 for a similar analysis on alongshore balance on sandy beach). The selected 5-day period, which covers small and large wave conditions over several tidal cycles, is representative of the typical residual variations. The increase in incoming wave energy on 13 May leads to a global increase of the magnitude of the momentum terms. The spatial distributions confirm the tendency revealed by Figure 6. Before the reef crest (CP2-CP3), the balance is dominated by the radiation stress and the slope terms, whereas the advective and friction terms are of lower magnitude. After the reef crest, the radiation stress contribution decreases while the friction effect increases. Tidal fluctuations are observed to affect the reef top dynamics (CP3-CP4), in particular for the slope term which oscillates with the periodic shifting of the surf zone. The magnitude of the residual, which represents the closure of the

balance, is larger around the reef top where wave dynamics and surface slope are strong. However, the tidal modulation of the residual suggests that some depth-related processes are missing to close the balance.

A final note relative to the hydrodynamic regimes observed across the reef barrier must be done. A series of peculiar points have been discarded from Figure 6. These points correspond to the strongest recorded waves, with H_s between 4 and 4.9 m observed during middle to high tide, and with SWL between 0.6 and 0.95 m. In such conditions, the momentum fluxes are clearly out of the typical range, that is, up to 60 and 80 $\text{N}\cdot\text{m}^{-3}$ for the advection and friction terms, respectively. The wave-induced current is so strong (about $2\text{ m}\cdot\text{s}^{-1}$), in particular at high tide, that the estimated Froude number $U/\sqrt{g(h+\bar{\eta})}$ above the reef flat reaches values close to 0.8, which is close to the transition to a supercritical regime, instead of values lower than 0.25 for all other conditions. Additionally, these events are associated to an increase (respectively a decrease) of CP2-CP3 (respectively CP3-CP4) slope terms, which indicates a strong lowering of the water level above the reef crest and a very strong friction. This confirms the transition from a critical to a supercritical hydrodynamic regime, at least around the reef top, during the most severe events. Such a regime is expected to have a drastic effect on reef hydrodynamics. Similar observations have been performed on tidal-driven reef currents (Lowe et al., 2015). The present study tends to indicate that strong waves alone are able to generate such an hydrodynamic transition. However, its detailed characterization would require a dedicated instrumentation, including local velocity measurements. These conditions are therefore not discussed further in the present paper.

3.4. Cross-Barrier Integration

The local evaluation of the depth-averaged momentum balance, that is, for successive sensor pairs, is sensitive to noise and measurement errors, as demonstrated by the relatively large scatter in Figure 6. A more robust analysis is obtained by integrating the momentum balance across the whole surveyed area (Buckley et al., 2015; Feddersen & Guza, 2003). The integration procedure followed to estimate each cross-reef integrated momentum term from the discrete measurements is described in Appendix A.

Figure 8 depicts the cross-reef integrated momentum balance between CP2 and CP5 for the 5-day event presented in Figure 7. The time series (Figure 8a) confirm the very weak contribution of the advection term. The integrated radiation and slope terms both show tidal oscillations, with a clear phase opposition. At high/low tide, more/less wave energy is propagating over the barrier, leading to an increase/decrease of the contribution of the radiation term. By contrast, the slope term is stronger at low tide. This is attributed to the global increase of friction for shallower water depths, leading to an enhanced bottom drag head loss. The residual is large, nearly of the order of slope and radiation terms, and related to the friction term. This unbalance between cross-reef integrated momentum fluxes highlights a bulk deficit of friction with the present parameterization. This is confirmed when plotting the sum of the advection, slope, and radiation terms as a function of the friction term (see Figure 8b): Part of the bottom friction is lacking to close the balance. Moreover, while the overall trend is rather well defined (determination coefficient 0.64), it does not have a zero intercept. This indicates the presence of a constant component in the residual in the cross-reef integrated momentum balance. Such offset is likely due to measurement uncertainties, in particular to instrument positioning.

To further quantify the deficit of friction in the integrated balance, the friction term was re-evaluated using an empirically derived constant bottom drag coefficient instead of the depth-varying one used previously. The best fit was obtained with $C_d = 0.06$ and is depicted in Figure 8d. This value is generally higher than the one obtained with equation (5), except for the shallower depths. Applying this a posteriori optimized C_d on the friction estimate decreases the residual magnitude (averaged over the 5-day period) by 85% but increases its standard deviation of about 150%. This is expected as the C_d inferred from the integrated momentum balance is a bulk estimate of friction across the monitored zone, ignoring any depth dependency or spatial variability of the reef structure. Furthermore, its estimate can be very sensitive to the presence of a constant residual in the balance.

The relative contributions of each integrated momentum term to the total momentum magnitude (see definition equation (A8), Appendix A) are plotted in Figures 8d-8g. Apart from the negligible contribution of advection, the contributions of the slope, the radiation, and the friction terms are nearly similar and of the order of 30% of the total magnitude. A finer inspection indicates a growing contribution of friction when the total momentum magnitude increases, while the slope contribution tends to saturate.

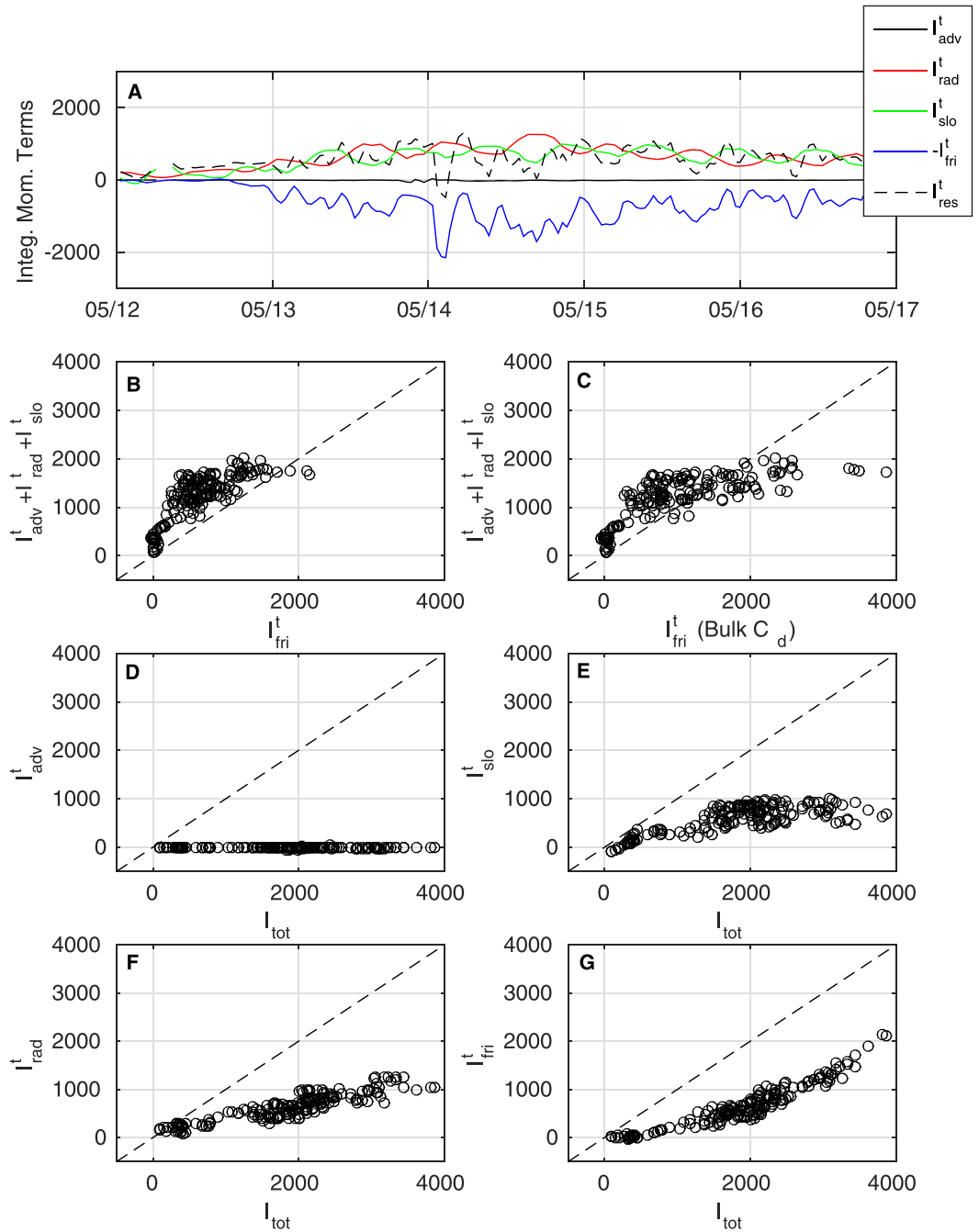


Figure 8. Cross-reef integrated momentum balance between CP2 and CP5 for the 5-day event. (a) Time series of the four integrated momentum terms and the residual (note that the integrated friction term I_{fri}^t is plotted negatively for the sake of visual commodity). (b) Sum of the advection, radiation, and slope terms versus the friction term. (c) Sum of the advection, radiation, and slope terms versus the empirical bulk- C_d friction term ($C_d = 0.06$). (d-g) The advection, slope, radiation, and friction terms versus the sum of the magnitude of all momentum terms, respectively.

3.5. Wave Setup

Figure 9 shows the reef top setup which is computed here as the difference between the 40-min averaged water level at CP3 and the still water level SWL. Overall setup values observed in our data set are lower than for the fringing reef cases studied by Becker et al. (2014). This difference is partly due to the presence of a wave-induced onshore-directed current, converting potential energy to kinetic energy. Furthermore, in the case of fringing reefs, the offshore-directed mean bottom stress (Buckley et al., 2016) tends to increase the

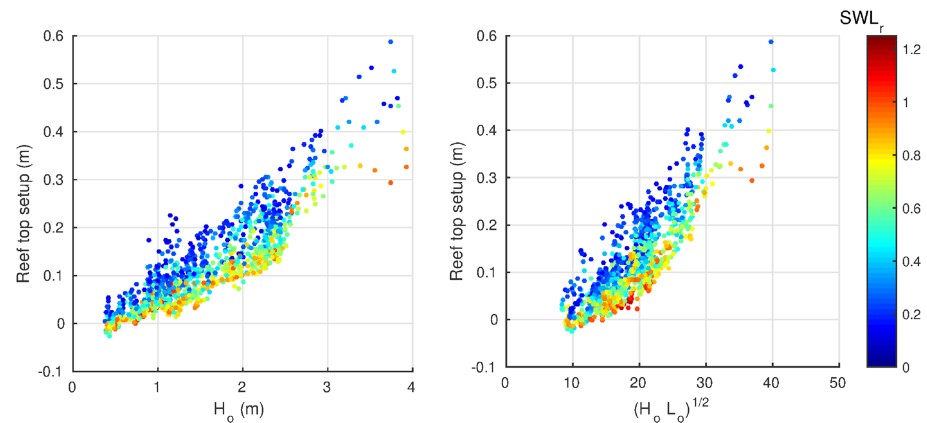


Figure 9. Setup at the reef top for May 2016 versus H_o (left), $\sqrt{H_o L_o}$ (right) where H_o and L_o are the deep water significant wave height and wave length. The setup is computed as the difference between the 40-min averaged water level at CP3 and the still water level. The color code depicts SWL_r , the (still) water depth above the reef top.

setup. By contrast, in our case, the onshore-directed mean bottom stress induces headloss (Dean & Bender, 2006), which contributes to lower the mean water level. The setup is plotted against H_o and $\sqrt{H_o L_o}$, where H_o and L_o are the deep water significant wave height and wave length linearly deshoaled from S4 forereef measurements (see Figure 3) in order to test the relationships widely used in empirical parameterizations for sandy beaches (Stockdon et al., 2006). In both cases, the color code represents the still water depth above the reef top (SWL_r). The results confirm the clear dependency on both incident wave height and water level (Becker et al., 2014). A better regression is however observed when plotting the setup against $\sqrt{H_o L_o}$ rather than against H_o alone, with determination coefficients of 0.83 and 0.77, respectively. The depth-dependency observed in Figure 9 is mainly attributed to forereef curvature (see section 4).

4. Discussion

The field observations provide a first-order overview of the depth-averaged momentum balance across the reef barrier. In order to gain more insights into the involved processes, numerical simulations are performed with the non-hydrostatic multilayer phase-resolving SWASH (Simulating Waves till SHore) model (Zijlema et al., 2011). A primary interest of such numerical simulations is to extend the studied area and increase the resolution in both horizontal and vertical directions. The model configuration is presented hereafter. Discussion points are then organized in three main topics: momentum balance, depth dependency, and vertical structure of the cross-reef currents.

4.1. Numerical Simulations

The phase-resolving wave model SWASH (Zijlema et al., 2011) is implemented along the studied cross-reef transect (2DV simulations) with 10 vertical layers. For each tested case, 30-min runs are performed over a 2.5 km domain ($-500 < X < 2,000$ m) extending from the outer forereef (30 m deep) at the open ocean boundary to the lagoon (10 m deep at $X = 2,000$ m). A 500-m wide sponge layer is imposed at the lagoon shoreward boundary. The horizontal resolution is 1 m. A 5-min spinup period is applied before recovering the model output each 0.25 s. The model is forced by a Joint North Sea Wave Observation Project spectrum based on the measured wave peak period T_p , while the offshore significant wave height is adjusted, following the procedure of Sous et al. (2019), to fit the forereef S4 measurement in 7-m depth. This ensures to get the correct wave input at the entrance of the considered system. The model is purely cross-shore, which means that wave directional spreading is not accounted for.

All model parameters are set to default values. A $K-\epsilon$ turbulence model is used to provide a fine description of the vertical turbulent fluxes. At the bottom boundary, the law of the wall is applied. The near-bed velocity is determined by the log-law while both K and ϵ are derived from the constant bottom stress. The approach used to mimic the reef roughness effect is not to impose an increased bottom drag coefficient but to combine a smooth-bed friction (Manning coefficient 0.01) and a porous layer imposed above the bed. In the porous layer, an additional dissipation is included in the horizontal momentum equation (Rijnsdorp & Zijlema,

Table 1

Comparison Between Model Prediction (Model) and Field Measurements (Meas.) for Cases Ref, A1, and A2 at Five Locations Across the Reef

	Offshore		CP2		CP3		CP4		CP5		AQP1	
	H_a	T_p	SWL	H_s	MWL	H_s	MWL	H_s	MWL	H_s	MWL	Q
	(m)	(s)	(m)	(m)	(m)	(m)	(m)	(m)	(m)	(m)	(m)	(m ² /s)
Ref Meas.	2.4	11.4	0.31	0.65	0.44	0.37	0.5	0.26	0.44	0.14	0.38	0.57
Ref Model	2.4	11.4	0.31	0.66	0.43	0.44	0.43	0.31	0.4	0.19	0.36	0.55
A1 Meas.	2.4	11.4	0.55	0.81	0.67	0.52	0.73	0.37	0.68	0.21	0.63	0.95
A1 Model	2.4	11.4	0.55	0.78	0.65	0.53	0.66	0.38	0.64	0.25	0.62	0.66
A2 Meas.	2.4	10.9	-0.03	0.54	0.19	0.26	0.26	0.17	0.18	0.09	0.1	0.21
A2 Model	2.4	10.9	-0.03	0.53	0.19	0.32	0.18	0.2	0.15	0.11	0.11	0.33

Note. The significant wave height corresponds to the short-wave band between 0.05 and 0.3 Hz.

2016) following the parameterization of Madsen (1983). Visual observations across the barrier showed a significant variability of the reef geometry with a very rough forereef, a compact reef top and a backreef covered by smaller coral boulders (0.1–0.2 m) on a dead coral bed with scattered but larger pinnacles, see underwater pictures in Sous et al. (2019). In order to keep consistency with the field data analysis, a spatially constant bottom drag parameterization is used, with a porous layer of constant height (0.3 m) and porosity of 0.9 applied on the bottom all across the barrier. This value has been calibrated on the reference case to obtain the best overall prediction for wave height, water level, and transport. Note that with the present approach based on a near-bed porous layer to represent the reef friction, the results are nearly insensitive to the choice of the bottom drag coefficient.

The model is tested against three different sets of observations, as listed in Table 1. The reference case is taken around mid-tide on 29 May. Significant wave height and peak period were 2.4 m and 11.4 s, respectively. Two additional cases, A1 and A2, with similar significant wave height but occurring at high and low tides, respectively, were identified and simulated for comparisons with the Reference case. The wave height was the same for the three cases, while the peak period is slightly lower for A2, with $T_p = 10.9$ s. The SWL was 0.31, 0.55, and -0.03 m for Ref, A1, and A2, respectively. For each case, forcing parameters, numerical outputs, and corresponding observations are given in Table 1.

A good agreement is found between measurements and simulations in terms of wave transformation, mean water level, and net transport (see also Figure 10 for reference case). The mean absolute errors for the significant wave height, mean water level and transports are 0.032 m, 0.033 m, and 0.14 m²·s⁻¹, respectively.

For each model run, the four momentum terms of equation (1) are computed using the depth- and time-averaged numerical outputs across the complete barrier cross-shore profile. The friction term is based on the log-based formulation of the bottom drag coefficient defined in equation (5).

Although the absolute errors between the model-based and observation-based momentum terms compared in Figure 10 are significant (up to 20 N·m⁻³), the cross-reef evolution of each term is well represented by the model. The overall agreement is also quite satisfactory for the vertical flow structure discussed in section 4.4. The present model configuration will therefore be used in the following sections to provide further insight on the physical processes revealed by the field data analysis.

4.2. Detailed Spatial Variability of the Momentum Balance

Figure 10 compares the model outputs for the reference case to the field data. The cross-shore profile of depth-averaged velocity is reconstructed from the transport measured at AQP1. A satisfactory agreement is obtained with the local measurement performed at SIG. Note that computing the numerical momentum terms in the exact same manner as done with the field data, that is, computing the gradients with the numerical data extracted at the field measurements positions, provides very close results to the continuous cell-by-cell computations presented in Figure 10. Overall, the model provides a fair description of the Short Wave transformation and MWL variations across the reef barrier. The residual is generally weak when compared to the momentum terms, see Figure 10e. This confirms the overall validity of the depth-averaged momentum equation introduced in equation (1). The remaining residual results from the combination of all hypotheses used to estimate the wave- and depth-averaged momentum terms from the wave-resolving 2DV

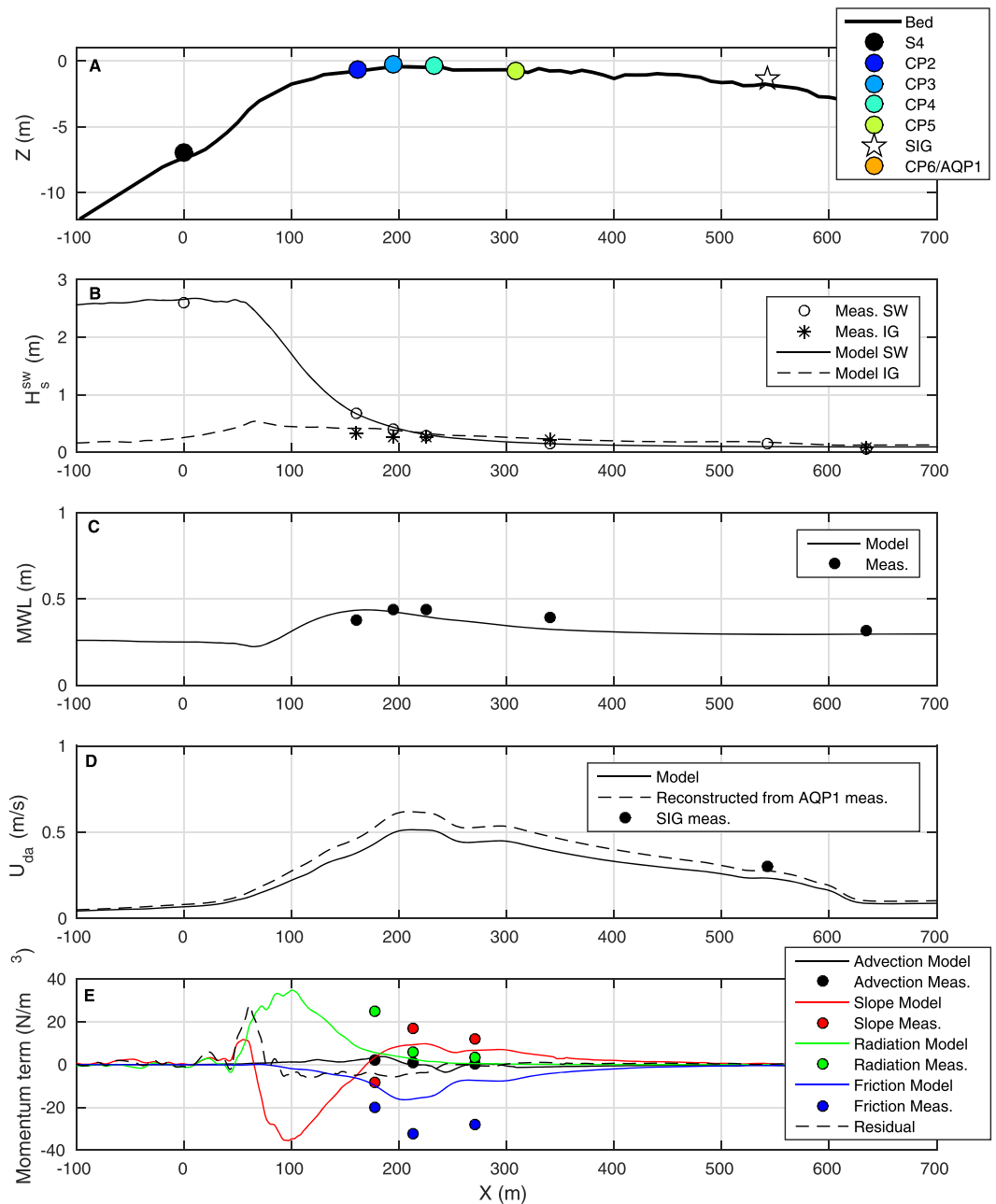


Figure 10. Numerical simulation for the reference case. The cross-shore profile of measured depth-averaged velocity is inferred from the transport observed at AQP1 divided by the local depth across the barrier.

numerical outputs, in particular the use of linear theory for the radiation stresses, the friction parameterization and the assumption of hydrostatic pressure (Martins et al., 2020). As expected, the strongest residual is observed near the breaking point, where the previous assumptions are affected by the high wave steepness.

Most SW energy is attenuated before the reef crest through the combination of breaking and frictional dissipation as well as energy transfer toward lower frequency Infragravity motions (Figure 10b). The MWL displays a weak shoaling-induced setdown offshore of the breakpoint, a setup through most of the surf zone and finally a progressive decrease across the reef flat (Figure 10c). This behavior contrasts with the nearly constant MWL observed on fringing reefs (Buckley et al., 2014, 2016). One notes that the reeftop setup is slightly underestimated in the simulation. The depth-averaged current strongly increases together with MWL in the surf zone and keep increasing at a lower rate over the reef flat to reach a maximum value of

$0.6 \text{ m}\cdot\text{s}^{-1}$ before decreasing across the back reef (Figure 10d). The comparison of the overall cross-shore evolution of momentum fluxes presented in Figure 10e confirms the experimental observations illustrated by Figure 6. The slope and radiation stress terms from Equation (1) are clearly dominant at the start of the surf zone, see Figure 10e. However, following the increase in onshore-directed current, the bottom friction term progressively increases over the forereef. As both the setup and the radiation stress gradient decrease in this area, the friction becomes the dominant momentum flux just before the reef top. The simulated momentum fluxes are compared with the estimations provided by in situ measurements for the considered case. Keeping in mind the limitations of the estimation of momentum fluxes from the present field data and their low resolution of horizontal positioning, a satisfactory overall agreement is found in terms of signs, trends, and orders of magnitude. The main discrepancy is observed for the numerical friction term, which is in good agreement with measurements near the reef top but tends to be locally smaller between CP4 and CP5 (Figure 10e). Local variations of the reef structure may explain such discrepancy, but further in situ investigations are required to address this issue.

Figure 10 highlights the progressive shift from a wave-dominated state in the surf zone toward a current- and friction-dominated state across the reef flat and backreef. Several additional lessons can be drawn from the series of supplementary test cases and the comparisons with field measurements listed in Table 1. First, the model is not able to precisely represent the effect of water level on the reef hydrodynamics with the present model settings. This tendency is for instance highlighted by comparing Ref, A1, and A2 for which the wave forcing is quite similar and the tide is middle, high, and low, respectively. Overall, the model tends to over (respectively under) estimate the wave height over the reef at low (respectively high) tide. This is also true for the transport. The effect of incoming wave energy on the barrier reef hydrodynamics is correctly represented by the model in terms of wave and mean water level, but the simulated transports show significant difference with the measurements.

4.3. Depth-Dependency of the Momentum Fluxes

Field measurements at the reef top highlighted a strong depth dependency of setup (Figure 9). This feature is also observed in the simulations, see for instance cases A1, Ref, and A2 taken respectively at high, middle, and low tides for similar wave conditions (Figure 11). The measured reef top setups, that is, the local difference between MWL (Mean Water Level) and SWL at CP3, are 0.2, 0.23, and 0.3 m while the corresponding simulated values are 0.13, 0.16, and 0.28 m, respectively. Thus, while the reef top setup is underestimated by the model, the depth dependency is properly predicted. Possible causes of such dependency are discussed below.

Wave reflection at the forereef could vary with the reef submergence depth, which could in turn affect wave dynamics over the reef flat and thus wave setup. To assess the role of wave reflection, incident and reflected wave energy are calculated using the Pressure and collocated horizontal velocity components method (Drevard et al., 2009) from the model outputs at $X = 0 \text{ m}$. The values of wave energy reflection coefficient are around 1% irrespective of the tidal phase. Such low values, which are in the same range than the observations of Péquignet et al. (2011) at the Ipan fringing reef or during the laboratory experiments of Yao et al. (2012), discard any significant influence of incoming wave reflection in the control of reef wave setup.

The role of forereef curvature can be assessed from Figure 11 which shows the comparison of each momentum term at high (A1), middle (Ref), and low (A2) tidal stages. The key driver of the increase in wave setup for decreasing water depth, seen in the slope term, is the increase of radiation stress gradient. This result reveals the role of forereef curvature in the wave energy dissipation, as hypothesized by Becker et al. (2014). The forereef is concave downward. As a result, the dimensionless slope is larger at low tide, allowing steeper waves to develop prior to breaking (Buckley et al., 2014; Ting & Kirby, 1994). This leads to a higher wave height-to-depth ratio at breaking during low tide with an increased wave dissipation and gradient in radiation stress, which in turn promotes a higher setup for low water levels. This effect can be quantified by the wave-height-to-depth ratio, which reaches maximal values of 0.8, 0.75, and 0.73 for A2, Ref, and A1, respectively. The reverse process has been observed for concave upward profile on steep rock cliffs (Dodet et al., 2018). For our site, this mechanism is expected to be sensitive to the incoming wave height, with a greater response for moderate wave conditions during which breaking occurs on the most curved portion of the forereef. This process is correctly captured by SWASH for the studied cases. However, simpler approaches based on a single wave-height-to-depth ratio for triggering the wave breaking would be a priori unable to represent

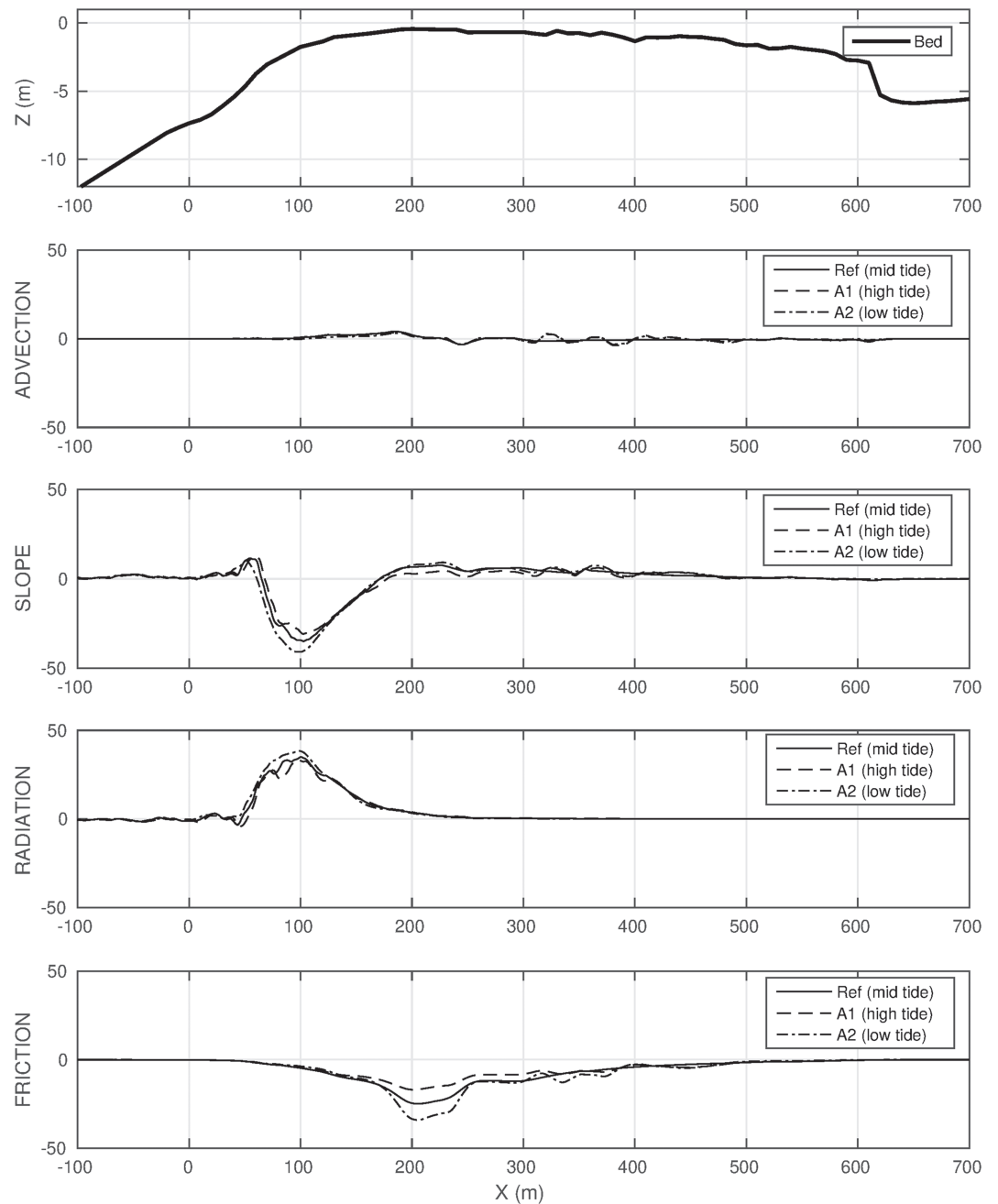


Figure 11. Tide control on momentum flux terms from equation (1). A1, Ref, and A2 cases correspond to high, middle, and low tides, respectively, with similar wave forcing.

the curvature effect on the wave transformation and its consequences in terms of setup or wave-induced current.

Finally, an additional possible contribution to the observed depth dependency is the tidal fluctuations of bottom friction. This is usually taken into account in the depth-averaged momentum balance using a decreasing C_d with decreasing depth following Manning-like or log-based formulations (McDonald et al., 2006; Pomeroy et al., 2012) which remain to be validated in the coral reef context (Rosman & Hensch, 2011). The present vertically resolved approach based on a porous layer over the bed allows to capture part of the depth-dependency, but further in situ measurements are needed to test the ability of the model to capture the tidal and spatial variability of bottom stress and turbulent fluxes.

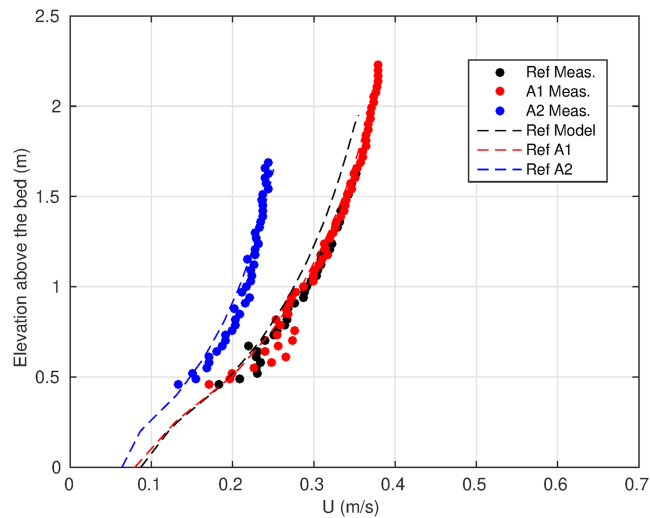


Figure 12. Vertical profiles of cross-shore velocity at SIG position. Comparison between experimental (dots) and numerical model (lines) for Ref, A1, and A2.

4.4. Vertical Structure of the Cross-Reef Current

In addition to the cross-reef transport, the vertical structure of the velocity above the canopy is of particular interest. The correct representation of shear and turbulent diffusion is indeed of primary importance to understand mixing and transport processes, which includes the dynamics of sediments, nutrients, pollutants, larvae, plankton, and so forth. Figure 12 depicts the good agreement between the measured velocity profile at SIG position and the numerical predictions of the 10-layer SWASH configuration.

Preliminary tests (not shown here) have been performed with a simpler model configuration, combining the 10-layer structure with a standard Manning friction formulation and an additional background viscosity.

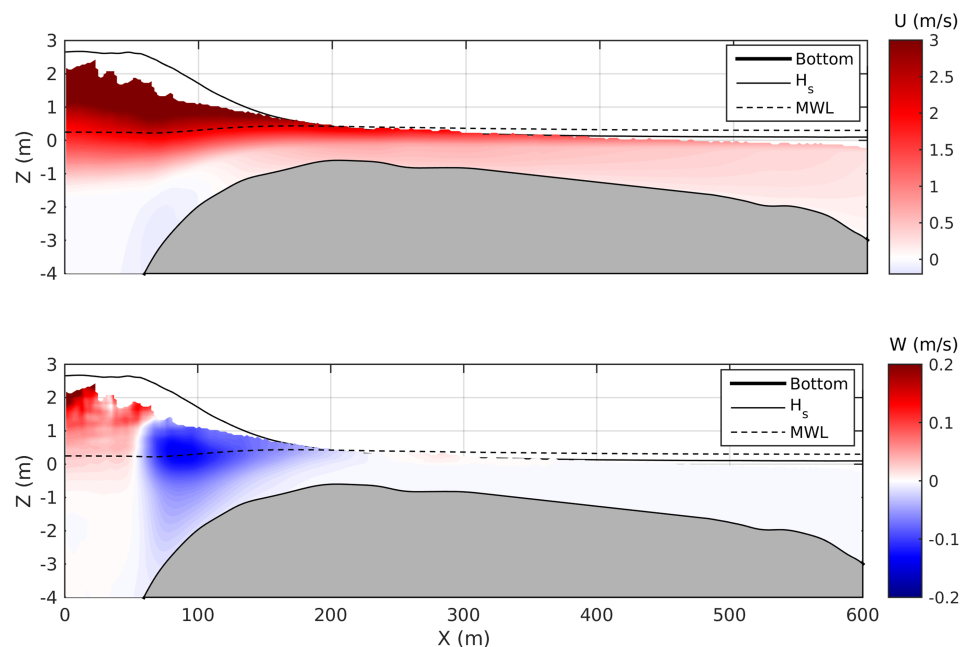


Figure 13. Time-averaged velocity structure across the reef barrier computed by the numerical model for reference case. Contours of time-averaged horizontal and vertical components of velocity are depicted in top and bottom plots, respectively. For reference, the cross-shore evolution of the mean water level and of the significant wave height are indicated in dashed and solid lines, respectively.

They show a drastic overestimation of the shear in the water column, with surface velocity largely exceeding the measured ones. A much better agreement is obtained here with the present configuration, which combines a $K - \epsilon$ turbulence model with a porous structure to simulate the reef. Such approach finely captures the displacement height as well as the overall shape and magnitude of the measured profile, while simultaneously giving a good description of the wave dynamics above the reef.

The model is used to analyze the time-averaged 2DV structure of velocity across the reef barrier. Note first that the upper limit of the velocity contours in Figure 13 is constrained by the wave-induced fluctuations of the free surface. More specifically, the highest elevation at which the mean velocity is displayed corresponds to the maximum crest elevation. From the reeftop and all across the backreef, the horizontal component of velocity is strongly sheared, in agreement with the profiles depicted in Figure 12. The vertical component is weak, showing small fluctuations related to the bottom undulations. A more complex velocity structure is observed above the forereef. Wave breaking is associated to the development of a consistent circulation cell with a downward flow under the core of the surf zone, being stronger in the upper part of the water column. It is associated with bottom return flow in the offshore part of the surf zone. This observation should be related to the undertow current widely documented on sandy beach systems (Faria et al., 2000; Feddersen & Guza, 2003; Greenwood & Osborne, 1990; Petitjean et al., 2016; Putrevu & Svendsen, 1993; Reniers et al., 2004). The main difference is that here only a portion of the onshore volume flux is returned in the undertow because of the onshore transport over the reef. The present instrumentation was not appropriate to confirm the simulated flow field and dedicated experiments should be engaged to get a more precise view of the circulation pattern in this hard-to-access and rough area. The presence of such striking feature is likely to affect the idealized depth-averaged momentum balance over the forereef and contribute to the magnitude of the wave setup (Gu erin et al., 2018). In addition, one can expect that it plays a significant role in the mixing and exchanges of water masses and nutrients between the forereef and the reef barrier.

5. Conclusion

Understanding the momentum balance over reef barriers is of primary importance for a number of reasons in the context of global change and increased human pressure, including shore protection and the quality of reef-lagoon ecosystems. Building on the pioneer conceptual works of Hearn (1999), Symonds et al. (1995), and Gourlay and Colleter (2005) and prior field observations of momentum dynamics in coral reef systems (Hench et al., 2008; Lentz et al., 2016, 2017; Lowe et al., 2009; Monismith et al., 2013), this study provides strong field evidences of the robustness of the depth-averaged momentum balance over a barrier reef. The analysis is based on a 2-month field experiment conducted at the Ouano reef barrier. Local estimates of the momentum balance are used to provide a spatial description of each momentum term fluctuations with tide and wave forcing evolution. Cross-reef integration of the momentum balance allows to quantify the relative contributions of each process and the momentum residual. The integrated advection momentum flux is very weak while the contributions of free surface slope, gradient of radiation stress, and bottom friction are of the same order of magnitude. A residual is observed, mainly attributed to the lack of precision of the bottom friction parameterization and to the measurement and positioning uncertainties. Additional numerical simulations based on a wave-resolving multilayer non-hydrostatic model (SWASH) are performed to extend and refine the studied area. Within the breaking zone over the forereef, the dominant processes are the breaking-induced decrease of significant wave height and the wave setup, that is, the increase of mean water level. Such feature is a classical observation on mild slope sandy beaches (Longuet-Higgins & Stewart, 1962). A major difference with sandy beaches arises when moving onshore within the inner surf zone: The wave-induced barotropic pressure gradient induces the development of an onshore-directed cross-reef current. The related bottom friction progressively increases and become dominant from the reef top. The associated headloss is therefore responsible for a setback across the reef flat and backreef. The advective momentum flux is generally negligible excepted near the reef top where it can represent up to about 10% of the momentum balance.

The cross-reef momentum balance is strongly depth dependent, with low (respectively high) water levels inducing higher (respectively lower) bottom friction and larger (respectively smaller) gradients of radiation stress in the breaking zone, which explains the tidal fluctuations of wave setup over the reef top. Once calibrated, the phase-resolving wave model SWASH is able to reproduce the cross-reef hydrodynamics, including wave attenuation, mean water level, and current. Such type of models, or their Boussinesq-based counterparts (Yao et al., 2019), appear as useful tools to anticipate the combined effects of global reef degradation

and sea level rise, which are major threats for low-lying areas. The present results confirm the overall validity of the depth-averaged momentum balance when aiming to predict wave setup and wave-induced transport, keeping in mind the importance of depth dependency and spatial variation of bottom friction in such complex and rough environments.

Appendix A: Cross-reef integration of the depth-averaged momentum balance

The momentum balance from equation (1) is first rewritten as

$$-\rho(\bar{\eta} + h) \frac{\partial}{\partial x}(U^2) - g\rho(\bar{\eta} + h) \frac{\partial \bar{\eta}}{\partial x} - \frac{\partial S_{xx}}{\partial x} = \bar{\tau}, \quad (\text{A1})$$

and then integrated between pairs of neighboring locations across the reef a and b . In the following, it is assumed that the water depth varies linearly between a and b , such that $\frac{\partial \bar{\eta}}{\partial x}$ and $\frac{\partial h}{\partial x}$ are constant (and do not depend on x). Using integration by parts and trapezoidal integration, the integrated advection and slope terms between locations a and b can be written as

$$I_{ab}^{adv} = - \int_a^b \rho(\bar{\eta} + h) \frac{\partial}{\partial x}(U^2) dx = -\rho \left(U_b^2(h_b + \bar{\eta}_b) - U_a^2(h_a + \bar{\eta}_a) - (h_b - h_a + \bar{\eta}_b - \bar{\eta}_a) \frac{U_a^2 + U_b^2}{2} \right), \quad (\text{A2})$$

and

$$I_{ab}^{slo} = - \int_a^b g\rho(\bar{\eta} + h) \frac{\partial \bar{\eta}}{\partial x} dx = -\rho g \left(\bar{\eta}_b^2 - \bar{\eta}_a^2 + h_b \bar{\eta}_b - h_a \bar{\eta}_a - \frac{\bar{\eta}_b + h_b - \bar{\eta}_a - h_a}{2} (\bar{\eta}_a + \bar{\eta}_b) \right), \quad (\text{A3})$$

respectively. The integrated radiation term can be more directly estimated as

$$I_{ab}^{rad} = - \int_a^b \frac{\partial S_{xx}}{\partial x} dx = S_{xxa} - S_{xxb}, \quad (\text{A4})$$

while the friction term is obtained by trapezoidal integration:

$$I_{ab}^{fri} = \int_a^b \bar{\tau} dx = \frac{\bar{\tau}_b + \bar{\tau}_a}{2} (x_b - x_a). \quad (\text{A5})$$

Each term is first integrated between each successive sensor pair (CP2-CP3, CP3-CP4, and CP4-CP5) and then summed across the complete area, for instance for the slope term

$$I_t^{slo} = I_{23}^{slo} + I_{34}^{slo} + I_{45}^{slo}. \quad (\text{A6})$$

The residual of the integrated momentum balance is given by

$$I_t^{res} = I_t^{adv} + I_t^{slo} + I_{45}^{rad} - I_t^{fri}. \quad (\text{A7})$$

Finally, in order to measure the relative contributions to the total balance, a total momentum magnitude is computed as the sum of each term magnitude:

$$I_{tot} = |I_t^{adv}| + |I_t^{slo}| + |I_{45}^{rad}| + |I_t^{fri}|. \quad (\text{A8})$$

Acknowledgments

This study was sponsored by the EC2CO OLZO program (CNRS INSU), the OLZO and CROSS-REEF Action Sud (MIO IRD), and the ANR project MORHOC'H (ANR-13-ASTR-0007). The Noumea IRD center and the GLADYS group supported the experimentation. GD is supported by ESA under the Sea State CCI project. Marcel Zijlema is warmly thanked for his insight on SWASH. We are grateful to all the contributors involved in this experiment.

The presented data are available at <https://doi.org/10.6084/m9.figshare.8966075.v1>; for more information contact the corresponding author.

References

- Andréfouët, S., Pages, J., & Tartinville, B. (2001). Water renewal time for classification of atoll lagoons in the Tuamotu archipelago (French Polynesia). *Coral Reefs*, 20(4), 399–408.
- Angwenyi, C. M., & Rydberg, L. (2005). Wave-driven circulation across the coral reef at Bamburi lagoon, Kenya. *Estuarine, Coastal and Shelf Science*, 63(3), 447–454.
- Becker, J., Merrifield, M., & Ford, M. (2014). Water level effects on breaking wave setup for Pacific island fringing reefs. *Journal of Geophysical Research: Oceans*, 119, 914–932. <https://doi.org/10.1002/2013JC009373>
- Bonneton, P., Lefebvre, J.-P., Bretel, P., Ouillon, S., & Douillet, P. (2007). Tidal modulation of wave-setup and wave-induced currents on the Aboré coral reef, New Caledonia. *Journal of Coastal Research*, 50, 762–766.
- Buckley, M., Lowe, R., & Hansen, J. (2014). Evaluation of nearshore wave models in steep reef environments. *Ocean Dynamics*, 64(6), 847–862.

- Buckley, M., Lowe, R. J., Hansen, J. E., & Van Dongeren, A. R. (2015). Dynamics of wave setup over a steeply sloping fringing reef. *Journal of Physical Oceanography*, *45*(12), 3005–3023.
- Buckley, M., Lowe, R. J., Hansen, J. E., & Van Dongeren, A. R. (2016). Wave setup over a fringing reef with large bottom roughness. *Journal of Physical Oceanography*, *46*(8), 2317–2333.
- Chevalier, C., Devenon, J.-L., Rougier, G., & Blanchot, J. (2014). Hydrodynamics of the Toliara reef lagoon (Madagascar): Example of a lagoon influenced by both waves and tide. *Journal of Coastal Research*, *31*, 1403–1416. <https://doi.org/10.2112/JCOASTRES-D-13-00077.1>
- Chevalier, C., Sous, D., Devenon, J.-L., Pagano, M., Rougier, G., & Blanchot, J. (2015). Impact of cross-reef water fluxes on lagoon dynamics: A simple parameterization for coral lagoon circulation model, with application to the Ouano lagoon, New Caledonia. *Ocean Dynamics*, *56*, 1509–1534. <https://doi.org/10.1007/s10236-015-0879-x>
- Dean, R. G., & Bender, C. J. (2006). Static wave setup with emphasis on damping effects by vegetation and bottom friction. *Coastal Engineering*, *53*(2-3), 149–156.
- Dodet, G., Bertin, X., Bruneau, N., Fortunato, AndréB, Nahon, A., & Roland, A. (2013). Wave-current interactions in a wave-dominated tidal inlet. *Journal of Geophysical Research: Oceans*, *118*, 1587–1605. <https://doi.org/10.1002/jgrc.20146>
- Dodet, G., Leckler, F., Sous, D., Ardhuin, F., Suanez, S., & Filipot, J.-F. (2018). Wave runup over the steep rocky cliffs of Banneg island, France. *Journal of Geophysical Research: Oceans*, *123*, 7185–7205. <https://doi.org/10.1029/2018jc013967>
- Dreverd, D., Rey, V., & Fraunié, P. (2009). Partially standing wave measurement in the presence of steady current by use of coincident velocity and/or pressure data. *Coastal Engineering*, *56*(9), 992–1001.
- Faria, A., Thornton, E., Lippmann, T., & Stanton, T. (2000). Undertow over a barred beach. *Journal of Geophysical Research*, *105*(C7), 16,999–17,010.
- Feddersen, F., & Guza, R. (2003). Observations of nearshore circulation: Alongshore uniformity. *Journal of Geophysical Research*, *108*(C1), 3006. <https://doi.org/10.1029/2001JC001293>
- Feddersen, F., Guza, R., Elgar, S., & Herbers, T. (1998). Alongshore momentum balances in the nearshore. *Journal of Geophysical Research*, *103*(C8), 15,667–15,676.
- Gawehn, M., van Dongeren, A., van Rooijen, A., Storlazzi, C. D., Cheriton, O. M., & Reniers, A. (2016). Identification and classification of very low frequency waves on a coral reef flat. *Journal of Geophysical Research: Oceans*, *121*, 7560–7574. <https://doi.org/10.1002/2016JC011834>
- Gourlay, M. R. (1996). Wave set-up on coral reefs. 1. set-up and wave-generated flow on an idealised two dimensional horizontal reef. *Coastal Engineering*, *27*(3), 161–193.
- Gourlay, M. R., & Colleter, G. (2005). Wave-generated flow on coral reefs: an analysis for two-dimensional horizontal reef-tops with steep faces. *Coastal Engineering*, *52*(4), 353–387.
- Greenwood, B., & Osborne, P. D. (1990). Vertical and horizontal structure in cross-shore flows: An example of undertow and wave set-up on a barred beach. *Coastal Engineering*, *14*(6), 543–580.
- Guérin, T., Bertin, X., Coulombier, T., & de Bakker, A. (2018). Impacts of wave-induced circulation in the surf zone on wave setup. *Ocean Modelling*, *123*, 86–97.
- Guza, R. T., & Thornton, E. B. (1981). Wave set-up on a natural beach. *Journal of Geophysical Research*, *86*, 4133–4137.
- Hearn, C. J. (1999). Wave-breaking hydrodynamics within coral reef systems and the effect of changing relative sea level. *Journal of Geophysical Research*, *104*(C12), 30,007–30,019.
- Hench, J. L., Leichter, J. J., & Monismith, S. G. (2008). Episodic circulation and exchange in a wave-driven coral reef and lagoon system. *Limnology and Oceanography*, *53*(6), 2681.
- Hoeke, R. K., Storlazzi, C. D., & Ridd, P. V. (2013). Drivers of circulation in a fringing coral reef embayment: A wave-flow coupled numerical modeling study of hanalei bay, hawaii. *Continental Shelf Research*, *58*, 79–95.
- Kench, P., & McLean, R. (2004). Hydrodynamics and sediment flux of hwa in an indian ocean atoll. *Earth Surface Processes and Landforms*, *29*(8), 933–953.
- Kraines, S. B., Suzuki, A., Yanagi, T., Isobe, M., Guo, X., & Komiyama, H. (1999). Rapid water exchange between the lagoon and the open ocean at majuro atoll due to wind, waves, and tide. *Journal of Geophysical Research*, *104*(C7), 15,635–15,653.
- Kraines, S. B., Yanagi, T., Isobe, M., & Komiyama, H. (1998). Wind-wave driven circulation on the coral reef at bora bay, miyako island. *Coral Reefs*, *17*(2), 133–143.
- Lentz, S. J., Churchill, J. H., & Davis, K. A. (2018). Coral reef drag coefficients surface gravity wave enhancement. *Journal of Physical Oceanography*, *48*(7), 1555–1566.
- Lentz, S. J., Churchill, J. H., Davis, K. A., Farrar, J. T., Pineda, J., & Starczak, V. (2016). The characteristics and dynamics of wave-driven flow across a platform coral reef in the red sea. *Journal of Geophysical Research: Oceans*, *121*, 1360–1376. <https://doi.org/10.1002/2015JC011141>
- Lentz, S. J., Davis, K. A., Churchill, J. H., & DeCarlo, T. M. (2017). Coral reef drag coefficients—Water depth dependence. *Journal of Physical Oceanography*, *47*(5), 1061–1075.
- Locatelli, F., Sous, D., Rey, V., Chevalier, C., Bouchette, F., Touboul, J., & Devenon, J.-L. (2017). Wave transformation over the ouano reef barrier, New Caledonia. In *Proceedings of coastal dynamics 2017, helsingor, 12-16 june*, pp. 356–367.
- Longuet-Higgins, M. S. (2005). On wave set-up in shoaling water with a rough sea bed. *Journal of Fluid Mechanics*, *527*, 217–234.
- Longuet-Higgins, M. S., & Stewart, R. (1962). Radiation stress and mass transport in gravity waves, with application to surf beats. *Journal of Fluid Mechanics*, *13*(4), 481–504.
- Lowe, R. J., Falter, J. L., Bandet, M. D., Pawlak, G., Atkinson, M. J., Monismith, S. G., & Koseff, J. R. (2005). Spectral wave dissipation over a barrier reef. *Journal of Geophysical Research*, *110*, C04001. <https://doi.org/10.1029/2004JC002711>
- Lowe, R. J., Falter, J. L., Monismith, S. G., & Atkinson, M. J. (2009). Wave-driven circulation of a coastal reef-lagoon system. *Journal of Physical Oceanography*, *39*(4), 873–893.
- Lowe, R. J., Leon, A. S., Symonds, G., Falter, J. L., & Gruber, R. (2015). The intertidal hydraulics of tide-dominated reef platforms. *Journal of Geophysical Research: Oceans*, *120*, 4845–4868. <https://doi.org/10.1002/2015JC010701>
- Lugo-Fernández, A., Roberts, H., Wiseman Jr, W., & Carter, B. (1998). Water level and currents of tidal and infragravity periods at tague reef, st. croix (usvi). *Coral Reefs*, *17*(4), 343–349.
- Madsen, P. (1983). Wave reflection from a vertical permeable wave absorber. *Coastal Engineering*, *7*(4), 381–396.
- Martins, K., Bonneton, P., Mouragues, A., & Castelle, B. (2020). Non-hydrostatic, non-linear processes in the surf zone. *Journal of Geophysical Research: Oceans*, *125*, e2019JC015521. <https://doi.org/10.1029/2019JC015521>
- Massel, S., & Gourlay, M. (2000). On the modelling of wave breaking and set-up on coral reefs. *Coastal Engineering*, *39*(1), 1–27.

- McDonald, C., Koseff, J., & Monismith, S. (2006). Effects of the depth to coral height ratio on drag coefficients for unidirectional flow over coral. *Limnology and Oceanography*, *51*(3), 1294–1301.
- Monismith, S. G. (2007). Hydrodynamics of coral reefs. *Annual Review of Fluid Mechanics*, *39*, 37–55.
- Monismith, S. G., Herdman, L. M., Ahmerkamp, S., & Hench, J. L. (2013). Wave transformation and wave-driven flow across a steep coral reef. *Journal of Physical Oceanography*, *43*(7), 1356–1379.
- Péquignet, A.-C., Becker, J., Merrifield, M., & Boc, S. (2011). The dissipation of wind wave energy across a fringing reef at Ipan, Guam. *Coral Reefs*, *30*(1), 71–82.
- Petitjean, L., Sous, D., Rey, V., Bouchette, F., Sabatier, F., & Meulé, S. (2016). The structure of nearshore currents driven by changes in meteo-marine forcings. *Coastal Engineering Proceedings*, *1*(35), 5.
- Pomeroy, A. W. M., Lowe, R. J., Ghisalberti, M., Storlazzi, C., Symonds, G., & Roelvink, D. (2017). Sediment transport in the presence of large reef bottom roughness. *Journal of Geophysical Research: Oceans*, *122*, 1347–1368. <https://doi.org/10.1002/2016JC011755>
- Pomeroy, A. W. M., Lowe, R., Symonds, G., Van Dongeren, A., & Moore, C. (2012). The dynamics of infragravity wave transformation over a fringing reef. *Journal of Geophysical Research*, *117*, C11022. <https://doi.org/10.1029/2012JC008310>
- Putrevu, U., & Svendsen, I. A. (1993). Vertical structure of the undertow outside the surf zone. *Journal of Geophysical Research*, *98*(C12), 22,707–22,716.
- Reidenbach, M. A., Monismith, S. G., Koseff, J. R., Yahel, G., & Genin, A. (2006). Boundary layer turbulence and flow structure over a fringing coral reef. *Limnology and Oceanography*, *51*(5), 1956.
- Reniers, A., Thornton, E., Stanton, T., & Roelvink, J. (2004). Vertical flow structure during sandy duck: observations and modeling. *Coastal Engineering*, *51*(3), 237–260.
- Rijnsdorp, D. P., & Zijlema, M. (2016). Simulating waves and their interactions with a restrained ship using a non-hydrostatic wave-flow model. *Coastal Engineering*, *114*, 119–136.
- Roeber, V., & Cheung, K. F. (2012). Boussinesq-type model for energetic breaking waves in fringing reef environments. *Coastal Engineering*, *70*, 1–20.
- Roelvink, D., Reniers, A., Van Dongeren, A., de Vries, J. v. T., McCall, R., & Lescinski, J. (2009). Modelling storm impacts on beaches, dunes and barrier islands. *Coastal Engineering*, *56*(11), 1133–1152.
- Rosman, J. H., & Hench, J. L. (2011). A framework for understanding drag parameterizations for coral reefs. *Journal of Geophysical Research*, *116*, C08025. <https://doi.org/10.1029/2010JC006892>
- Sous, D., Chevalier, C., Devenon, J.-L., Blanchot, J., & Pagano, M. (2017). Circulation patterns in a channel reef-lagoon system, Ouano Lagoon, New Caledonia. *Estuarine, Coastal and Shelf Science*, *196*, 315–330.
- Sous, D., Tissier, M., Rey, V., Touboul, J., Bouchette, F., Devenon, J.-L., et al. (2019). Wave transformation over barrier reefs. *Continental Shelf Research*, *184*, 66–80. <https://doi.org/10.1016/j.csr.2019.07.010>
- Stockdon, H. F., Holman, R. A., Howd, P. A., & Sallenger Jr, A. H. (2006). Empirical parameterization of setup, swash, and runup. *Coastal Engineering*, *53*(7), 573–588.
- Storlazzi, C. D., Elias, E. P., & Berkowitz, P. (2015). Many atolls may be uninhabitable within decades due to climate change. *Scientific Reports*, *5*, 14546.
- Symonds, G., Black, K. P., & Young, I. R. (1995). Wave-driven flow over shallow reefs. *Journal of Geophysical Research*, *100*(C2), 2639–2648.
- Taebi, S., Lowe, R. J., Pattiaratchi, C. B., Ivey, G. N., Symonds, G., & Brinkman, R. (2011). Nearshore circulation in a tropical fringing reef system. *Journal of Geophysical Research*, *116*, C02016. <https://doi.org/10.1029/2010JC006439>
- Tartinville, B., Deleersnijder, E., & Rancher, J. (1997). The water residence time in the Mururoa Atoll Lagoon: Sensitivity analysis of a three-dimensional model. *Coral Reefs*, *16*(3), 193–203.
- Tartinville, B., & Rancher, J. (2000). Wave-induced flow over Mururoa Atoll reef. *Journal of Coastal Research*, *16*, 776–781.
- Ting, F. C., & Kirby, J. T. (1994). Observation of undertow and turbulence in a laboratory surf zone. *Coastal Engineering*, *24*(1-2), 51–80.
- Van Dongeren, A., Lowe, R., Pomeroy, A., Trang, D. M., Roelvink, D., Symonds, G., & Ranasinghe, R. (2013). Numerical modeling of low-frequency wave dynamics over a fringing coral reef. *Coastal Engineering*, *73*, 178–190.
- Vetter, O., Becker, J. M., Merrifield, M. A., Péquignet, A.-C., Aucan, J., Boc, S. J., & Pollock, C. E. (2010). Wave setup over a pacific island fringing reef. *Journal of Geophysical Research*, *115*, C12066. <https://doi.org/10.1029/2010JC006455>
- Wolanski, E., Delesalle, B., Dufour, V., Aubanel, A., et al. (1993). Modeling the fate of pollutants in the Tiahura Lagoon, Moorea, French Polynesia. In *11th australasian conference on coastal and ocean engineering: Coastal engineering a partnership with nature; preprints of papers*, Institution of Engineers, Australia, pp. 583.
- Yao, Y., Huang, Z., Monismith, S. G., & Lo, E. Y. (2012). Characteristics of monochromatic waves breaking over fringing reefs. *Journal of Coastal Research*, *29*(1), 94–104.
- Yao, Y., Zhang, Q., Chen, S., & Tang, Z. (2019). Effects of reef morphology variations on wave processes over fringing reefs. *Applied Ocean Research*, *82*, 52–62.
- Zijlema, M., Stelling, G., & Smit, P. (2011). SWASH: An operational public domain code for simulating wave fields and rapidly varied flows in coastal waters. *Coastal Engineering*, *58*(10), 992–1012.